Optics Communications 520 (2022) 128401

Contents lists available at ScienceDirect

Optics Communications

journal homepage: www.elsevier.com/locate/optcom

Tomographic single pixel spatial frequency projection imaging

Patrick Stockton [a], Gabe Murray [b], Jeffrey J. Field [c,a], Jeff Squier [d], Ali Pezeshki [a,e], Randy A. Bartels [a,f,*]

[a] Department of Electrical and Computer Engineering, Colorado State University, Fort Collins, CO 80523, USA
[b] Department of Physics, Colorado State University, Fort Collins, CO 80523, USA
[c] Center for Imaging and Surface Science, Colorado State University, Fort Collins, CO 80523, USA
[d] Department of Physics, Colorado School of Mines, Golden, CO 80401, USA
[e] Department of Mathematics, Colorado State University, Fort Collins, CO 80523, USA
[f] School of Biomedical Engineering, Colorado State University, Fort Collins, CO 80523, USA

ARTICLE INFO

Keywords:
Computational imaging
Single pixel imaging
Tomography
Super resolution
Coherent imaging
Holography

ABSTRACT

Conventional methods for three-dimensional (3D) imaging frequently rely on voxel-by-voxel data acquisition, which restricts the range of specimens in which they can be effectively employed. While advances in imaging technology now permit the routine acquisition of 3D images approaching video rates, there are other limitations to image formation in fluorescent microscopy that prohibit studies in large volume samples, highly scattering media, and dynamic environments. Some approaches to 3D image collection circumvent this need by the use of tomographic imaging, where sub-3D projections are collected at varying illumination angles and reconstructed through an inversion algorithm to compute an estimate of the 3D fluorophore distribution. Many such methods rely on spatially coherent light, and thus prohibit the use of fluorescent light. By employing unique spatio-temporally varying illumination patterns in conjunction with computational imaging approaches to image reconstruction, we show that some limitations of laser scanning and wide-field imaging can be overcome. We outline several approaches that utilize tomographic projections with patterned illumination to collect 3D image data. All three dimensional optical imaging exploits projection of the desired 3D information into a lower-dimensional subspace, and then a full three dimensional object is estimated from these data. We discuss a number of such single pixel strategies that project object information onto a zero-dimensional, usually a power, measurement. Further, we outline computational image reconstruction approaches that enhance the object estimates by employing a forward model for the image formation process.

1. Introduction

Optical microscopy is a powerful method for studying a wide range of samples with minimal perturbation to the system under study. The simplest imaging methodologies rely on a segmented detector, such as a camera chip, to record the intensity of a widefield image that is formed with a series of optical components [1,2]. Widefield imaging is highly developed, relatively inexpensive, and widely available. Despite the numerous advantages, this technology is still limited — preventing its use in a broad set of applications. For example, widefield imaging is difficult or impossible in spectral regions that lack high quality segmented detectors, such as the mid-infrared and terahertz bands [3,4]. In some environments, the optical properties of the specimen, such as absorption and scattering, may obscure regions of the specimen, making imaging of desired object features challenging.

In scenarios where widefield imaging is challenging, it is often advantageous to form images through single pixel imaging. The most common forms of single pixel imaging are based on laser scanning microscopy (LSM), where a laser (or other spatially coherent beam) is focused to a small point and raster scanned through a specimen. These methods include confocal microscopy and multiphoton-excited fluorescent microscopy [5–7]. In LSM, the relative position of the focused excitation beam is translated throughout the specimen and a fraction of the signal power is measured for each illumination position. LSM opens capabilities for imaging within specimens that suffer from optical scattering, but at the expense of slow image formation.

The speed of LSM imaging is limited due to the fact that signal is serially acquired from each spatial point. Imaging speed is improved by applying delocalized illumination light (see Fig. 1), rather than raster scanning a tightly focused beam [8–13]. While delocalized illumination allows signal to be gathered from across the specimen, thereby improving imaging speed, the sequence of illumination patterns must be suitably designed to enable full recovery of the object from knowledge of the illumination patterns and the set of measurements [11,14–18].

* Corresponding author at: Department of Electrical and Computer Engineering, Colorado State University, Fort Collins, CO 80523, USA.
E-mail address: randy.bartels@colostate.edu (R.A. Bartels).

https://doi.org/10.1016/j.optcom.2022.128401
Received 1 April 2021; Received in revised form 12 December 2021; Accepted 25 April 2022
Available online 30 April 2022
0030-4018/

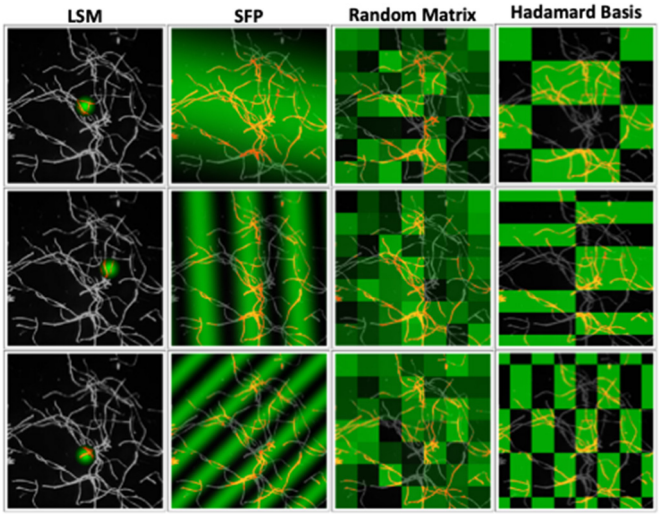

Fig. 1. Conceptual diagram of several single pixel imaging modalities. The green pattern represents a spatial modulation of the illumination light intensity. Separate modulation strategies are shown in columns. Moving left to right these are: laser scanning (confocal or nonlinear) microscopy, single frequency projection, random matrices, and Hadamard matrices. The rows show snapshots of illumination patterns that evolve over time; the required set of patterns depend on the mathematical properties of the illumination patterns, and for full imaging coverage, the average illumination must cover the entire image field of view. In the case of fluorescent emission, the total signal for each illumination pattern is proportional to the total emitted fluorescent power, and each of those power measurements can be viewed as an inner product between the spatial distribution of the molecular concentration, $c(\mathbf{x}_\perp)$, which is the desired object, and the illumination light pattern, $I_j(\mathbf{x}_\perp)$, to produce a signal that is proportional to the inner product of the two spatial distributions, $\langle c(\mathbf{x}_\perp), I_j(\mathbf{x}_\perp)\rangle_{\mathbf{x}_\perp}$.

Most delocalized single pixel techniques use a sequence of illumination patterns that are uncorrelated spatially across the object — using either random illumination patterns [15,19], Hadamard matrices [14], or spatial frequency structured light [11,20–22], to name a few. Particular excitement has accompanied the recognition that when the object is sparse in some basis, accurate image estimates can be obtained through application of compressive sensing principles [19,23,24].

In addition to improvements in imaging speed, modulated single pixel imaging has been applied to increase the information extracted, as well as to expand the range of accessible contrast mechanisms. Modulated single pixel illumination has been applied to many spatial and spectral modalities to access numerous contrast mechanisms for imaging, such as nonlinear excitation [8,25–27], to obtain super resolution imaging [25], spectroscopy through wavelength labeling [28,29] or compressive sensing [30,31], quantitative phase information [26,32], simulation of coherent propagation of incoherent light emission [21, 33], and diffuse optical spectroscopic imaging [34,35]. The advantages of imaging in the mid infrared [36] and terahertz [37] spectral regions have also been demonstrated.

With single pixel imaging, it becomes necessary to combine the knowledge of the illumination patterns, the physics of the signal contrast mechanism, and a forward model for the single pixel image data formation, and then solve the inverse problem to estimate the underlying object — the spatial distribution of the signal contrast mechanism.

Generally, single pixel imaging is framed as a computational imaging problem, where a forward model provides an expected signal, $\mathcal{D}\{c(\mathbf{x})\}(t)$. Here, $\mathcal{D}\{\cdot\}$ is the forward operator that maps object information, $c(\mathbf{x})$, interrogated by the illumination intensity, $I_{\text{ill}}(t)$, at time t onto a scalar signal value that is related to the average power captured by the detector, $\Phi(t)$. In an experiment, data is acquired as a vector of discrete samples of the signal. The discrete measurement vector $[\mathbf{y}]_i = \Phi(t_i)\,\Delta t + [\epsilon]_i$ is based on the expected signal sampled at time t_i with a sample averaging time Δt. The signal is corrupted by noise introduced by the illumination source and detection electronics in the measurement, denoted by ϵ_i for the ith sample. Noise from different areas of the sample are assumed to be mutually independent.

Delocalized single pixel imaging may benefit from an improved signal-to-noise ratio (SNR) depending on the dominant source of noise [38,39]. The SNR will be improved by multiplexing the photon counts together with the use of a single pixel detector if the signal is detector noise limited (thermal, electronic, or $1/f$ noise). On the other hand, if the signal is shot noise limited, multiplexing the photon counts together will result in decreased SNR; however, these deficiencies can be largely mitigated with suitable computational imaging algorithms.

To estimate the object spatial distribution, a model fitting problem may be posed to find the best fit (e.g., in least-squares sense) between the measured data and the signal, modeled using the forward operator applied to the estimated object. This model fitting problem is typically posed as a finite dimensional optimization problem for finding an N-point discrete approximation $\mathbf{c} \in \mathbb{R}_+^N$, on some pre-selected spatial grid, to the object spatial distribution $c(\mathbf{x})$. If the forward operator is a linear integral operator, as is the case in many applications, then its action on $c(\mathbf{x})$ at any time instant t can be approximated as the inner product between the discretized object distribution $\mathbf{c}$ and a vector $\mathbf{a}_t$ that depends on the kernel of the forward operator: $\mathcal{D}\{c(\mathbf{x})\}(t) \approx \mathbf{a}_t^T\,\mathbf{c}$.

Let t_i denote the ith sampling time, y_i be the intensity measurement at time t_i, and $\mathbf{A}$ be a matrix whose ith row is $\mathbf{a}_{t_i}^T$. Then, the problem is to fit the linear model $\mathbf{A}\,\mathbf{c}$ to the measurement vector $\mathbf{y} = [y_1, y_2, \ldots, y_M]^T$, where M is the total number of temporal samples. An estimate $\hat{\mathbf{c}}$ of $\mathbf{c}$ is typically found thorough variations of least-squares fitting, sometimes with regularization:

$$\hat{\mathbf{c}} := \underset{\mathbf{c}>0}{\arg\min}\ \|\mathbf{y} - \mathbf{A}\mathbf{c}\|_2 + \lambda\, R[\mathbf{c}]. \tag{1}$$

The regularization or penalty function $R[\cdot]$, weighted by the parameter λ, is included to force a solution that matches our prior knowledge about $\mathbf{c}$ (e.g., sparsity or smoothness) and to perform denoising. Many problems that we wish to solve are highly sensitive to noise due to their ill-possedness, requiring strong regularization to constrain the degrees of freedom of the solution [40–42]. In some cases, it is possible to express the estimate $\hat{\mathbf{c}}$ in closed-form by constructing appropriate inverse operators analytically. In other cases, one has to resort to numerical iterations. Over the past twenty years, many algorithms have been developed for various choices of the regularization function R. A review of such algorithms and optimization methods can be found in [43]. The effect of noise on the estimation depends on the choice of the regularization function and the specific algorithm used to solve (1). Of course, we always prefer to have an analytical form for the inverse operator (estimator map), associated with (1), for taking $\mathbf{y}$ to $\hat{\mathbf{c}}$, because we can then derive analytical error bounds for our estimates and quantify resolution limits. Also, when $\mathbf{A}$ is large or poorly conditioned, numerical iterations may suffer from a lack of stability or may require a large amount of memory and a large number of iterations to arrive at a good estimate [44–47].

In this article, we discuss single pixel tomographic computational imaging [33,48,49]. For two of our scenarios, we are able to find the inverse operators analytically and present closed-form expressions for the object estimate. For the others, we use numerical methods. The analyses of forward and inverse operators allows us to identify the imaging impulse response and spatial frequency support, which readily facilities comparison to conventional optical imaging methods.

2. Single pixel spatial frequency projection (SFP) imaging

2.1. Modulation of the field

Single pixel spatial frequency projection (SFP) imaging refers to a class of computational imaging methods that exploit illumination light that is modulated with a time-varying spatial frequency structure

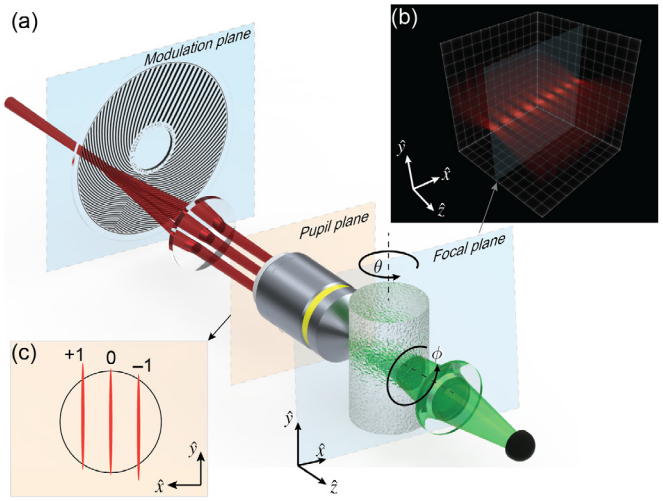

Fig. 2. (a) A schematic of a single pixel SFP tomographic imaging system. The light in the modulator plane, focused by a cylindrical lens, serves as the conjugate object plane for the illumination optical system and is imaged into the object region to the conjugate image plane, which is also called the focal plane. (b) An example of the illumination intensity for a particular modulation spatial frequency. (c) Filtering in the pupil plane plays a critical role in determining the 3D propagation of the spatially coherent modulated illumination field.

[11,20,21,50]. A general schematic of a SFP imaging system is shown in Fig. 2.

The incident light, $E_{inc}(x_\perp)$, is focused to a line by a cylindrical lens on the modulator, $M(\mathbf{x}_{\perp,\mathrm{mo}}, t)$. The modulated illumination light, $E_{\mathrm{mo}}(\mathbf{x}_{\perp,\mathrm{mo}})$, is produced by modifying spatially coherent light incident on a modulator, $E_{\mathrm{inc}}(\mathbf{x}_{\perp,\mathrm{mo}})$, so that the modulator imprints a transverse spatial modulation on the field amplitude. The coordinates of the plane where the modulator lies are denoted $\mathbf{x}_{\perp,\mathrm{mo}} = (x_m, y_m)$. The modulated illumination field is the product of the incident field and the modulator mask, giving the expression

$$E_{\mathrm{mo}}(\mathbf{x}_{\perp,\mathrm{mo}}; t) = E_{inc}(\mathbf{x}_{\perp,\mathrm{mo}}) m(\mathbf{x}_{\perp,\mathrm{mo}}; t).$$

In SFP imaging, the modulation patterns, $m(\mathbf{x}_{\perp,\mathrm{mo}}; t)$, are composed of sparse set of time varying spatial frequencies.

The modulated illumination radiant field, which is the spatial Fourier transform of the modulated field, is a convolution of the Fourier transform of the modulator mask,

$$M(\mathbf{k}_\perp; t) = \mathcal{F}\{m(\mathbf{x}_{\perp,\mathrm{mo}}; t)\} = \int m(\mathbf{x}_{\perp,\mathrm{mo}}; t) \exp(-i\,\mathbf{k}_\perp \cdot \mathbf{x}_{\perp,\mathrm{mo}})\, d^2\,\mathbf{x}_{\perp,\mathrm{mo}},$$

with the Fourier transform of the incident illumination light. The radiant field in the modulation plane then reads

$$\mathcal{E}_{\mathrm{mo}}(\mathbf{k}_\perp) = \mathcal{E}_{\mathrm{inc}}(\mathbf{k}_\perp) *_{\mathbf{k}_\perp} M(\mathbf{k}_\perp; t).$$

Here $\mathcal{E}_{\mathrm{inc}}(\mathbf{k}_\perp) = \mathcal{F}\{E_{\mathrm{inc}}(\mathbf{x}_{\perp,\mathrm{mo}})\}$ is the incident radiant field and $*_{\mathbf{k}_\perp}$ is the convolution operator with respect to $\mathbf{k}_\perp$, and $\mathbf{k}_\perp = (k_x, k_y)$ denotes the transverse spatial frequencies.

Since $E_{\mathrm{inc}}(\mathbf{x}_{\perp,\mathrm{mo}})$ illuminates only a portion of the modulator spatial extent, the spatial frequency representation of the modulator mask may be expressed as a sum, $M(\mathbf{k}_\perp; t) = \sum_j \alpha_j \exp[i\,\varphi_j(t)]\,\delta[\mathbf{k}_\perp - \mathbf{k}_{\perp,\mathrm{mo},j}(t)]$, over the discrete, time-varying modulation frequencies, $\mathbf{k}_{\perp,\mathrm{mo},j}(t)$, each of which has an amplitude of α_j. Some modulators are able to impart a phase shift, $\varphi_j(t)$, that varies as the transverse modulation spatial frequency, $\mathbf{k}_{\perp,\mathrm{mo},j}(t)$, evolves. This total radiant field is the sum $\mathcal{E}_{\mathrm{mo}}(\mathbf{k}_\perp) = \sum_j \alpha_j\, \mathcal{E}_{\mathrm{inc}}[\mathbf{k}_\perp - \mathbf{k}_{\perp,\mathrm{mo},j}(t)]$.

2.2. The three dimensional illumination field

The three-dimensional (3D) illumination pattern of a spatially coherent modulated field is dictated by the propagation and interference of that field. Assuming that the modulated field lies in the object conjugate plane of a 4-f illumination imaging system with a coherent transfer function (CTF) $\mathcal{H}(\mathbf{k}_\perp)$, we may compute the three dimensional illumination field in the object space by using the angular spectral propagator [1,51]. By adopting a Cartesian coordinate system in the object space $\mathbf{x} = (x, y, z)$, where $z = 0$ identifies the focal plane, we define z as the optical axis of the imaging system, and the nominal propagation direction of the light. Then, the wavevector component in the transverse plane relative to the optical axis is $\mathbf{k}_\perp = (k_x, k_y)$, with the full wavevector given as $\mathbf{k} = (k_x, k_y, k_z)$.

The modulated field is image relayed from the modulation plane to a conjugate image plane that resides in the object space (Fig. 2); we will refer to this as the focal plane ($z = 0$). The CTF of the illumination system imparts a low pass spatial frequency filter onto the illumination field, producing a radiant field in the focal plane of $\mathcal{E}_{\mathrm{ill}}(\mathbf{k}_\perp; 0) = \mathcal{H}(\mathbf{k}_\perp)\,\mathcal{E}_{\mathrm{mo}}(\mathbf{k}_\perp; 0)$. Since $M(\mathbf{k}_\perp; t)$ is represented by a discrete sum over transverse modulation frequencies, it follows that the illumination field in the focal plane is also represented by a discrete sum, $E_{\mathrm{ill}}(\mathbf{x}_\perp, 0; t) = \sum_j E^{(j)}_{\mathrm{ill}}(\mathbf{x}_\perp, 0; t)$. Here $\mathbf{x}_\perp = (x, y)$, in the object coordinates $\mathbf{x} = (x, y, z)$, where z is the optic axis of the imaging system.

At the focal plane, the jth radiant field $\mathcal{E}^{(j)}_{\mathrm{ill}}(\mathbf{k}_\perp; t)$ is the product of the modulated field in the pupil plane of the objective, $\alpha_j\,\mathcal{E}_{\mathrm{inc}}[\mathbf{k}_\perp - \mathbf{k}_{\perp,j}(t)]$, with the illumination optical system CTF, $\mathcal{H}(\mathbf{k}_\perp)$. In the spatial domain, this jth field term is obtained from the inverse Fourier transform, leading to

$$E^{(j)}_{\mathrm{ill}}(\mathbf{x}_\perp, 0; t) = \alpha_j\, \mathcal{F}^{-1}\{\mathcal{H}(\mathbf{k}_\perp)\,\mathcal{E}_{\mathrm{inc}}[\mathbf{k}_\perp - \mathbf{k}_{\perp,j}(t)]\}.$$

The filtering of the modulated radiant field, illustrated in Fig. 2(c), is the source of the variation in the peak field amplitude of each transmitted field at the origin, $\mathbf{x} = (0, 0, 0)$, of the object coordinate system. This amplitude is calculated by

$$a_j(t) = E^{(j)}_{\mathrm{ill}}(\mathbf{x}_\perp, 0; t)\Big|_{\mathbf{x}_\perp = \mathbf{0}} = \alpha_j \int \mathcal{H}(\mathbf{k}_\perp)\,\mathcal{E}_{\mathrm{inc}}[\mathbf{k}_\perp - \mathbf{k}_{\perp,j}(t)]\, d^2\,\mathbf{k}_\perp.$$

As we show later, $a_j(t)$ is related to the modulation transfer function of the single pixel SFP imaging system.

The filtering by the 4f illuminating imaging system can modify the propagation direction, i.e., the k-vector, of each of the modulation illumination terms. The direction of the jth illumination field is denoted by the vector $\mathbf{k}_j(t) = (k_{x,j}(t), k_{y,j}(t), k_{z,j}(t))$. The transverse beam center frequency components are determined by the centroid of the radiant field,

$$k_{(x,y),j}(t) = \frac{\int k_{(x,y)} \left|\mathcal{E}^{(j)}_{\mathrm{ill}}(\mathbf{k}_\perp; t)\right|^2 d^2\mathbf{k}_\perp}{\int \left|\mathcal{E}^{(j)}_{\mathrm{ill}}(\mathbf{k}_\perp; t)\right|^2 d^2\mathbf{k}_\perp}.$$

The axial spatial frequency of each wave is set by the dispersion relationship of the Helmholtz equation,

$$k_{z,j}(t) = \sqrt{k^2 - k^2_{x,j}(t) - k^2_{y,j}(t)}.$$

The amplitude, $a_j(t)$, and wavevector, $\mathbf{k}_j(t)$, are used to define a slowly varying three dimensional complex field envelope, $u_j(\mathbf{x}; t)$, where the rapidly varying phase, $\exp\left[i(\varphi_j(t) + \mathbf{k}_j(t) \cdot \mathbf{x})\right]$, is removed. The complex envelope is normalized to unity at the origin of the object coordinates,

$$u_j(\mathbf{x}; t) = \exp\left[-i(\varphi_j(t) + \mathbf{k}_j(t) \cdot \mathbf{x})\right]\; E^{(j)}_{\mathrm{ill}}(\mathbf{x}; t) / E^{(j)}_{\mathrm{ill}}(\mathbf{0}; t).$$

The three dimensional field, $E^{(j)}_{\mathrm{ill}}(\mathbf{x}; t)$, is computed using the angular spectral propagator to propagate the in-focus field at $z = 0$ to an arbitrary defocus plane z.

With this formalism, we find that the transverse spatial frequency spectrum of the normalized field envelope, $U_j(\mathbf{k}_\perp; z, t) = \mathcal{F}_{\mathbf{x}_\perp}\{u_j(\mathbf{x}; t)\}$, at the defocus distance, z, is given by

$$U_j(\mathbf{k}_\perp; z, t) = \frac{e^{-i[\varphi_j(t) + \mathbf{k}_j(t)\cdot\mathbf{x}]}}{a_j(t)}\, \mathcal{H}(\mathbf{k}_\perp)\,\mathcal{E}_{\mathrm{inc}}[\mathbf{k}_\perp - \mathbf{k}_{\perp,j}(t)]\, e^{i\,z\sqrt{k^2 - \|\mathbf{k}_\perp\|^2_2}}.$$

Here the wavenumber is the norm of the wavevector $k = \|\mathbf{k}\|_2 = 2\pi/\lambda$ and $\|\mathbf{k}_\perp\|_2^2 = k_x^2 + k_y^2$ is the square of the norm of the transverse wavevector.

Putting together all of the factors defined above, we have a total illumination field of $E_i(\mathbf{x}_\perp, 0; t) = \sum_j E_{\text{ill}}^{(j)}(\mathbf{x}_\perp, 0; t)$, where each field term is written as, $E_{\text{ill}}^{(j)} = a_j(t)\, u_j(\mathbf{x}; t)\, \exp\left[i(\varphi_j(t) + \mathbf{k}_j(t) \cdot \mathbf{x})\right]$. The time-variation of the field arises from a temporal variation in the modulator, which also imparts a continuously varying phase shift, $\varphi_j(t)$, that enables the separation of interfering terms in the illumination intensity $I_{\text{ill}}(\mathbf{x}, t) = \left|E_{\text{ill}}(\mathbf{x}, t)\right|^2$. Here, the dimensionality of the problem is set by the dimension of the spatial vector, $\mathbf{x} = (x, y, z)$.

2.3. SPIFI and CHIRPT

To illustrate the implementation of SFP imaging, we consider two limiting cases for the illumination field: plane wave and line focus (light sheet) illumination; the line focus case is illustrated in Fig. 2(b). We begin by analyzing the plane wave model. The number of terms in the summation are constrained by the modulator and the illumination system, with the most common being three beam, $j \in \{-1, 0, 1\}$, interference for SPatIal Frequency modulation for Imaging (SPIFI) imaging [11,52], and two beam, $j \in \{0, 1\}$, imaging for Coherent Holographic Image Reconstruction by Phase Transfer (CHIRPT) imaging [21,53–55].

Assuming a circular aperture in the pupil plane with a radial coherent cutoff spatial frequency of $k_c = k\,\text{NA}_{\text{ill}}$, and NA_{ill} is the numerical aperture of the imaging illumination system, the CTF may be written in the form $\mathcal{H}(\mathbf{k}_\perp) = \text{rect}[\|\mathbf{k}_{\perp,\text{mo},j}(t)\|_2/2\,k_c]$. The rect function evaluates to $\text{rect}(x) = 1$ for $|x| < 0.5$ and 0 otherwise. With a circular CTF, in the plane wave case [53], the modulated radiant incident field of the jth term is approximated as $\mathcal{E}_{\text{inc}}^{(j)}(\mathbf{k}_\perp, t) \approx \delta^2[\mathbf{k}_\perp - \mathbf{k}_{\perp,\text{mo},j}(t)]$. Thus, the modulated radiant field transmitted through the pupil of the illumination imaging system is approximated by

$$\mathcal{E}_{\text{ill}}^{(j)}(\mathbf{k}_\perp; z, t) = \delta^2[\mathbf{k}_\perp - \mathbf{k}_{\perp,\text{mo},j}(t)]\,\text{rect}[\|\mathbf{k}_{\perp,\text{mo},j}(t)\|_2/2\,k_c]\, e^{i\,z\sqrt{k^2 - \|\mathbf{k}_\perp\|_2^2}}.$$

In the plane wave model, the normalized field envelope is invariant with spatial coordinate, i.e., $u_j(\mathbf{x}; t) = 1$, and thus $a_j(t) = \alpha_j\,\text{rect}[\|\mathbf{k}_{\perp,\text{mo},j}(t)\|_2/2\,k_c]$, and $\mathbf{k}_j(t) = (\mathbf{k}_{\perp,\text{mo},j}(t) \cdot \hat{x}, \mathbf{k}_{\perp,\text{mo},j}(t) \cdot \hat{y}, \sqrt{k^2 - \|\mathbf{k}_{\perp,\text{mo},j}(t)\|_2^2})$. Here $\hat{x}$ and $\hat{y}$ are the unit vectors along the x and y coordinates, respectively.

By contrast, for a beam focused to a line [54,55] along the y direction with a spatial frequency modulation along the length of the line, which is denoted as the x direction, then we use $\mathbf{k}_{\perp,\text{mo},j} = (k_{x,mo,j}(t), 0)$. Assuming that the spatial frequency support along k_y is uniform, then the filtered radiant field of the jth field term for a circular CTF with coherent cutoff spatial frequency k_c is

$$\mathcal{E}_{\text{ill}}^{(j)}(\mathbf{k}_\perp; z, t) = \delta[k_x - k_{x,mo,j}(t)]\,\text{rect}[k_y/k_\ell(t)]\, e^{i\,z\sqrt{k^2 - \|\mathbf{k}_\perp\|_2^2}}.$$

Here, the height of the spatial frequency support along the k_y direction is the chord length, $k_\ell(t) = 2\,\text{Re}\left\{\sqrt{k_c^2 - k_{x,mo,j}^2(t)}\right\}$.

The amplitude of the jth field at the origin is $a_j(t) = \alpha_j\, k_\ell(t)/2\,\pi$ and because $k_{y,j} = 0$, the wavevector is $\mathbf{k}_j(t) = (k_{x,mo,j}(t), 0, \sqrt{k^2 - k_{x,mo,j}^2(t)})$. The diffracting light sheet beam envelope follows the dependence dictated by the integral

$$u_j(\mathbf{x}; t) = \frac{e^{-i\,z\sqrt{k^2 - k_{x,mo,j}^2(t)}}}{2\,\pi} \int \text{rect}\left(\frac{k_y}{k_\ell(t)}\right) e^{i\,k_y\,y}\, e^{i\,z\sqrt{k^2 - k_{x,mo,j}^2(t) - k_y^2}}\, d\,k_y.$$

While there is no general solution for this diffracting envelope, the solution in the focal plane ($z = 0$) is $u_j(\mathbf{x}; t) = k_\ell(t)\,\text{sinc}(k_\ell(t)\,y)/2\,\pi$, where $\text{sinc}(x) = \sin(\pi\,x)/\pi\,x$. This shows that the normalized field amplitude is uniform along x and that only the diffraction of the line focus into a light sheet, $u_j(y, z)$, is relevant to the changing of the illumination pattern.

2.4. Forward and inverse operators for SFP imaging

The forward model for SFP imaging with single pixel detection follows from the combination of the contrast mechanism, optical system, and the illumination patterns. The forward and inverse operators for SFP imaging for a number of single pixel tomographic imaging configurations are presented in the subsequent subsections. However, before we look at the specific operators, we develop a general framework for analyzing single pixel techniques. Our general framework will assume that full tomographic imaging can be performed where we scan along an additional coordinate ϕ to obtain information that spans the full dimension of the tomographic problem (i.e., the dimension of the $\mathbf{x}$ used). The scanning coordinate will be denoted by a subscript ϕ, which we set to zero to indicate when standard single pixel imaging is being performed.

In the previous section, we computed the three dimensional propagation of an illumination field modulated by a planar spatial light modulator. This propagating field presents a 3D illumination pattern to the object. In single pixel imaging, power from light that interacts with the object is recorded by a single pixel detector; this data is combined with the model of the signal collection of the contrast mechanism (e.g., absorption [11], linear scattering [49], fluorescent or luminescent emission [11,21,33], Raman scattering [27,30,31], or nonlinear interactions [21,25,27]) and the 3D light distribution to then solve the inverse problem using an inverse operator to estimate the object spatial distribution.

Earlier we defined a forward operator as the mathematical operation that mapped from the object spatial distribution, $c(\mathbf{x})$, to the signal collected by a single pixel photodetector $\boldsymbol{\Phi}_\phi(t)$. Often, a particular demodulated sideband will be extracted, and this serves as the expected signal that is predicted by the forward model, $\tilde{\boldsymbol{\Phi}}_\phi(t) = \mathcal{D}\{c(\mathbf{x})\}(t, \phi)$. The index ϕ will be used to indicate a sequence of measurements for tomographic imaging.

In SFP single pixel imaging, the forward model operator is defined by

$$\mathcal{D}\{c(\mathbf{x})\}(t, \phi) = \langle \beta(t) \boldsymbol{\Psi}_\phi(\mathbf{x}, t)\, c(\mathbf{x}) \rangle_{\mathbf{x}}. \tag{2}$$

Here we have neglected unimportant constants of proportionality that do not impact the image formation model. In addition, we are using Dirac integral notation of $\langle \cdot \rangle_{\mathbf{x}} = \int \cdot\, d^n\mathbf{x}$, where n is the dimension of the problem, defined by the dimension of $\mathbf{x}$. The forward operator is defined as a weighted inner product, $\langle \beta(t)\, f(t) \rangle_t$, with the weight, $\beta(t)$, denoting the fringe visibility at each time t, and thus each illumination transverse spatial frequency.

The function $\boldsymbol{\Psi}_\phi(\mathbf{x}, t)$ is the Fourier kernel of the forward operator that arises in SFP imaging from the interference of field terms that are isolated by the phase shifting terms, $\varphi_j(t)$. The weighting function $\beta(t)$ accounts for the spatial frequency support of the imaging, that is determined by the fringe visibility of the projected spatial frequencies and the tomographic scan parameter, ϕ, in SFP.

Acquired data, $\mathbf{y}$, are obtained from the sampled signal power and includes noise introduced by the measurement process. The acquired data can be inverted to obtain an object estimate by matching the data to the expected signal using Eq. (1). A common strategy is to solve this problem with iterative optimization, however, this approach often requires large computational resources.

When possible, using a closed form analytic model of the inverse operator to solve for the least squares estimate of the object from the set of data may provide an advantage in terms of computational complexity and computation time. The inverse operator is defined by

$$\hat{c}(\mathbf{x}) = \mathcal{D}^{-1}\{\tilde{\boldsymbol{\Phi}}_\phi(t)\}(\mathbf{x}) = \langle \tilde{\boldsymbol{\Psi}}_\phi^\dagger(\mathbf{x}, t)\, \tilde{\boldsymbol{\Phi}}_\phi(t) \rangle_{t,\phi}. \tag{3}$$

Here $\tilde{\boldsymbol{\Psi}}_\phi^\dagger(\mathbf{x}, t)$ is the dual kernel for the inversion. Ideally, this dual kernel is biorthogonal to the forward operator kernel, which we express mathematically as $\langle \boldsymbol{\Psi}_\phi(\mathbf{x}, t)\, \tilde{\boldsymbol{\Psi}}_\phi^\dagger(\mathbf{x}, t) \rangle_t = \delta^n(\mathbf{x})$.

In imaging systems, strict orthogonality may be only possible asymptotically, but the finite numerical aperture (NA) may lead to a compact function that is not a Dirac delta function. The forward and dual kernels are defined so as to be strictly orthogonal whenever possible. The function $\beta(t)$ is a term that physically describes the fringe visibility that is dictated by the finite transverse spatial frequency support enabled by the illumination objective lens, and thus accounts for the non-orthogonality due to the fact that a diffraction-limited spatial resolution exists. In SFP tomographic imaging, it is possible to find analytic expressions or approximate expansions for the dual kernel, and thus the inverse operator. In cases where this is not possible, we must resort to an iterative solution using Eq. (1).

With the definition of the inverse operator, we may describe the properties of the computational imaging system. The impulse response of the SFP computational imaging system, which we will call a point spread function (PSF) follows directly from substitution of Eq. (2) into Eq. (3), from which we may define the PSF as

$$\mathrm{PSF}(\mathbf{x}) = \frac{\left\langle \beta(t)\, \Psi_\phi(\mathbf{x}', t)\, \tilde{\Psi}_\phi^\dagger(\mathbf{x}' + \mathbf{x}, t) \right\rangle_{t,\phi}}{\left\langle \beta(t)\, \Psi_\phi(\mathbf{x}', t)\, \tilde{\Psi}_\phi^\dagger(\mathbf{x}' + \mathbf{x}, t) \right\rangle_{t,\phi,\mathbf{x}}}, \tag{4}$$

The PSF is normalized with $\int \mathrm{PSF}(\mathbf{x})\, d\mathbf{x} = 1$ to allow for a quantitative estimate of the object. The optical transfer function (OTF) follows from the Fourier transform of the PSF, $\mathrm{OTF} = \mathcal{F}\{\mathrm{PSF}(\mathbf{x})\}$. In the remainder of the article, we will develop the forward and inverse kernel functions, as well as calculate the PSF and OTF for a number of SFP single pixel computational tomographic imaging experiments.

The model in Eq. (2) is not completely general as it requires that the signal be recorded by the incoherent superposition of a signal power that is generated by the product of the illumination intensity, $I_{\mathrm{ill}}(\mathbf{x})$, and the local object contrast, $c(\mathbf{x})$. The model is valid for many common imaging modes, such as those that rely on fluorescent emission, spontaneous Raman scattering, and absorption contrast mechanisms. In the case of fluorescence [33,49] or spontaneous Raman scattering [30,31], $c(\mathbf{x})$ is the spatial distribution of the concentration of the molecules (fluorescent or Raman active). In the case of absorption, analysis of the signal with the generalized optical theorem [56] shows that the contrast is proportional to $c(\mathbf{x}) = \mathrm{Im}\{\eta(\mathbf{x})\}$, where we have assumed a uniform background refractive index and $\eta(\mathbf{x})$ which is the variation in optical susceptibility perturbation, of which the positive imaginary component contributes to optical absorption.

Another caveat is that our treatment in this article analyzes modulation of spatially coherent light. However, SFP computational imaging is not restricted to spatially coherent illumination light. Modulated spatially incoherent or partially coherent light can also be used, but there are additional considerations, such as localization of structured modulations near the focal plane. We stress that while we focus on illumination with spatially coherent spatio-temporally structured light, the detected light need not be spatially coherent, and we discuss cases for both spatially and temporally incoherent light collected on the single pixel detector.

Below, we consider a set of SFP imaging problems, and compute the least-squares estimate of the concentration, where we minimize the $\mathcal{L}^2$ norm error, of the object contrast distribution. The estimate of the object obtained by this strategy is denoted by $\hat{c}(\mathbf{x})$ that is computed by applying the inverse operator, $\mathcal{D}^{-1}$. The specific forward and inverse operators will be provided for several imaging scenarios explored below from which we obtain PSF and OTF functions for the imaging modalities.

3. CHIRPT imaging

Coherent Holographic Image Reconstruction by Phase Transfer (CHIRPT) imaging [21,53–55] uses two-beam interference. One beam is a non-scanned, time stationary reference beam, $j = 0$, propagating on the optic axis, $\mathbf{k}_{\perp,0} = (0,0)$. The second beam, $j = 1$, with $\mathbf{k}_{\perp,1} = (k_{x,1}(t), 0)$, linearly scans through all of the x-spatial frequencies supported by the NA of the illumination optics with the functional form of $k_{x,1}(t) = \gamma\, t$ at the modulation chirp rate $\gamma = k_c\, T^{-1}$. Here $k_c = k\, \mathrm{NA}_{\mathrm{ill}}$ is the coherent cutoff spatial frequency of the illumination imaging system with numerical aperture $\mathrm{NA}_{\mathrm{ill}}$ and $2T$ is the total modulation time. The two beams are brought to a tight line focus and interfere with each other to produce interference fringes which constitutes the projected spatial frequency, as shown in Fig. 2(b).

The Fourier kernel of the forward operator in CHIRPT is

$$\Psi^{\mathrm{CH}}(\mathbf{x}, t) = \rho_{0,1}(y, z)\, \exp\left[-i\, \Delta\mathbf{k}(t) \cdot \mathbf{x}\right], \tag{5}$$

where the spatial frequency used for imaging arises from the reference and scanning field wavevector difference, $\Delta\mathbf{k}(t) = \mathbf{k}_1(t) - \mathbf{k}_0$ and the weighting function in the forward operator is $\beta(t) = \mu(t)$. The amplitudes have been normalized so that $a_1(t) = a_0\, \mu(t)$, where $\mu(t) = k_\ell(t)/k_\ell(0) = \sqrt{1 - (t/T)^2}$ is the fringe visibility of the two interfering beams. The fringe visibility is a real quantity, which reflects the fact that $|t| \le T$. The spatial weighting distribution is $\rho_{i,j}(y, z) = u_i(y, z)\, u_j^*(y, z)$, and with the light sheet illumination considered here,

$$\Delta\mathbf{k}(t) = k \left(\frac{t}{T}\, \mathrm{NA}_{\mathrm{ill}}, 0, \sqrt{1 - \left(\frac{t}{T}\, \mathrm{NA}_{\mathrm{ill}} \right)^2} - 1 \right). \tag{6}$$

3.1. One-dimensional CHIRPT imaging

The simplest CHIRPT imaging arises from estimating a line image from the set of measurements where the illumination spatial frequency is varied along that same dimension. In such a case, we consider an object that is infinitesimally thin and located at a depth of z_0, so that $c(\mathbf{x}) \to \delta(z - z_0)\, c(\mathbf{x}_\perp)$. For this thin object

$$\mathcal{D}_{\mathrm{CH1D}}\{\bar{c}_{y_0}(x)\}(t) = \left\langle \beta(t)\, \Psi^{\mathrm{CH1D}}(x, t)\, \bar{c}_{y_0}(x) \right\rangle_x \tag{7}$$

where we have defined a 1D object averaged along the y direction for an illumination line centered on $y = y_0$ as

$$\bar{c}_{y_0}(x) = \int \rho_{0,1}(y, z_0)\, c(x, y + y_0)\, dy. \tag{8}$$

The 1D CHIRPT Fourier kernel is

$$\Psi^{\mathrm{CH1D}}(x, t) = \Psi^{\mathrm{CH}}(x, 0, z_0, t) = \rho_{0,1}(0, z_0)\, e^{-i\, \Delta k_x(t)\, x}\, e^{-i\, \Delta k_z(t)\, z_0}. \tag{9}$$

The difference frequencies used here are given in the vector elements in Eq. (6). Since the forward operator is simply a Fourier kernel, the dual kernel of the inverse operator, $\tilde{\Psi}^{\mathrm{CH1D}}(x, t) = \Psi^{\mathrm{CH1D}}(x, t)$, is the adjoint of the forward kernel.

The 1D CHIRPT line image is estimated by the expression

$$\hat{c}_{y_0}(x) = \mathcal{D}_{\mathrm{CH1D}}^{-1}\{\tilde{\Phi}(t)\}(x) = \left\langle \tilde{\Psi}^{\mathrm{CH1D},\dagger}(x, t)\, \tilde{\Phi}(t) \right\rangle_t. \tag{10}$$

The $\dagger$ denotes adjoint (complex-conjugate for Fourier kernel). The biorthogonality condition is verified by noting that $\langle \tilde{\Psi}^{\mathrm{CH1D}\dagger}(x', t) \Psi^{\mathrm{CH1D}}(x' + x, t) \rangle_t = 2T\, \sin(k\, \mathrm{NA}_{\mathrm{ill}}\, x)/k\, \mathrm{NA}_{\mathrm{ill}}\, x$. In the limiting case of infinite NA, this biorthogonal function becomes a Dirac delta function. It follows then that the PSF defined in Eq. (4) is given by

$$\mathrm{PSF}(x) = \frac{2\, J_1(k\, \mathrm{NA}_{\mathrm{ill}}\, x)}{k\, \mathrm{NA}_{\mathrm{ill}}\, x}.$$

where $J_1(\cdot)$ is the Bessel function of the first kind. The OTF is computed from the Fourier transform of the PSF, leading to

$$\mathrm{OTF}(k_x) = \mathrm{Re}\left\{ \sqrt{1 - (k_x/k_c)^2} \right\}.$$

The estimated 1D object obtained in Eq. (10) can be extended into a 2D object estimate to resolve an approximate representation of $c(\mathbf{x}_\perp)$ by taking a sequence of data traces for a set of y_i values. The individual 1D images are then stacked into a 2D image. This approach readily assembles a 2D image, yet along the y-direction, the spatial resolution is determined by the one dimensional autocorrelation of the coherent

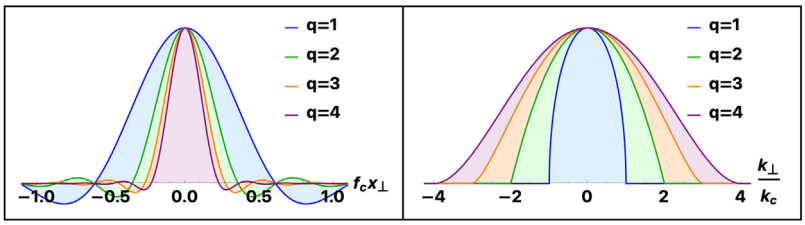

Fig. 3. SPIFI and CHIRPT line outs of the point spread functions (PSFs) and optical transfer functions (OTFs) for several SFP imaging orders: $q \in \{1, 2, 3, 4\}$ along x. The abscissa is normalized to be unitless and independent of NA and wavelength using the spatial frequency cutoff $f_c = \frac{NA}{\lambda}$, $k_c = 2\pi f_c$. The left panel shows SPIFI/CHIRPT PSFs for the first four SFP orders. The blue, green, orange, purple lines show the 1st, 2nd, 3rd, and 4th order PSFs relative to the spatial frequency cutoff f_c. The right panel shows the corresponding frequency support, OTFs relative to the coherent cutoff spatial frequency k_c. The 2D plot of the first and second order OTF is shown in Fig. 13 where the asymmetry along y can be observed.

transfer function along the y direction for each projected x spatial frequency. As a result, spatial frequency support is not isotropic, and the y-direction fails to benefit from super-resolution imaging enhancements, demonstrated with nonlinear excitation [25], that benefit spatial resolution for imaging along the modulated direction.

Under these conditions, the phase shifting term that acts as a carrier frequency for isolation of interfering terms accumulates phase at a multiple q given by the harmonic order: $\varphi(t) \rightarrow q\,\varphi(t)$. Similarly, the Fourier kernel accumulates an amplified spatial frequency modulation rate: $\mathbf{\Delta k}(t) \rightarrow q\,\mathbf{\Delta k}(t)$, so that the q^{th}-order Fourier kernel scales as $\Psi^{\text{SFP(q)}}(\mathbf{x}, t) \propto \exp\left[-i\,q\,\mathbf{\Delta k}(t)\cdot\mathbf{x}\right]$. Along 1D, the qth order CHIRPT OTF is

$$\text{OTF}_q(k_x) = \left(\text{Re}\left\{\sqrt{1-\left(\frac{k_x}{q\,k_c}\right)^2}\right\}\right)^q.$$

An analytic expression for the qth order PSF can be directly computed, but it is represented in terms of cumbersome hypergeometric functions. Plots of the PSF and OTF are shown in Fig. 3 for orders $q = 1-4$.

3.2. SPIFI imaging

Spatial frequency modulation for imaging (SPIFI) imaging uses three interfering beams [11,25,27,30] and carries the advantage of being easy to implement with a simple transmission mask. More interference terms arise from the presence of the additional beam giving first and second order modulation bands that appear near the first order and second order harmonic modulation frequencies. The first order, $q = 1$, SPIFI kernel is

$$\Psi^{\text{SP(1)}}(\mathbf{x}, t) = w_{01}(y, z; t)\,\cos\left[\Delta k_z(t)\,z - \varphi_\rho(y, z; t)\right]\,\exp(-i\,\Delta k_x(t)\,x), \tag{11}$$

and the kernel for second order SPIFI is

$$\Psi^{\text{SP(2)}}(\mathbf{x}, t) = \rho_{-1,1}(y, z; t)\,e^{-i\,2\,\Delta k_x(t)\,x}. \tag{12}$$

We have defined variables to track the magnitude, $w_{i,j}(y, z; t) = |\rho_{i,j}(y, z; t)|$, and phase, $\varphi_{\rho_{i,j}}(y, z; t) = \angle\rho_{i,j}(y, z; t)$, of the complex bounding envelope $\rho_{i,j}(y, z; t)$. SPIFI can be applied to 1D and 2D imaging in scenarios similar to CHIRPT, but with slightly modified kernels in the forward and inverse operators. In fact, at the focal plane ($z = 0$), the SPIFI and CHIRPT operators are identical, with the exception that SPIFI also contains a forward operator with double the spatial frequency support of the first order SPIFI and CHIRPT bands. At the focal plane, the PSF and OTF for SPIFI are the same as the result for 1D CHIRPT for $q = 1$.

In the case of the second order, $q = 2$, SPIFI term, then the PSF is

$$\text{PSF}_2(x) = \frac{\sin(2\,k\,\text{NA}_{\text{ill}}\,x) - 2\,k\,\text{NA}_{\text{ill}}\,x\,\cos(2\,k\,\text{NA}_{\text{ill}}\,x)}{2\,k^2\,\text{NA}_{\text{ill}}^2\,\pi\,x^3}. \tag{13}$$

The OTF for the second order SPIFI term reads

$$\text{OTF}_2(k_x) = \left(\text{Re}\left\{\sqrt{1-\left(\frac{k_x}{2\,k_c}\right)^2}\right\}\right)^2, \tag{14}$$

where we have used the fringe visibility term $\beta(t) = \mu^2(t)$. Note that we provided the OTF and PSF for the general qth order in-focus CHIRPT and SPIFI in the previous section.

3.2.1. Two-dimensional (2D) transverse CHIRPT and SPIFI imaging

CHIRPT and SPIFI imaging along one direction can be extended to 2D transverse imaging in several ways. We analyze the imaging properties of 1D CHIRPT extended to 2D CHIRPT with a simple line scan [11]. In the case of 2D transverse CHIRPT [32], we will consider a thin object located at the plane z_0, given by $c(\mathbf{x}) = \delta(z - z_0)\,c(\mathbf{x}_\perp)$. Our analysis is restricted to the in-focus imaging case, where $z_0 = 0$. At the focal plane, the 2D CHIRPT kernel is given by

$$\Psi^{\text{CH2D}}(x, t) = \rho_{0,1}(y, 0; t)\,e^{-i\,\Delta k_x(t)\,x}. \tag{15}$$

The envelope, $\rho_{0,1}(y, 0; t)$, varies in time because the spatial frequency support of the +1 term along k_y varies with time, leading to the expression

$$\rho_{0,1}(y, 0; t) = \text{sinc}\left(k_c\,y\right)\,\text{sinc}\left(k_c\,y\sqrt{1-\left(\frac{t}{T}\right)^2}\right). \tag{16}$$

An analytic inverse operator for the single pixel imaging with the kernel given in Eq. (16) is not known. As a result, the conventional strategy for accumulating line images estimated with 1D CHIRPT reconstruction as given by Eq. (10) for each scan position y_0 into a 2D image is to stack them in a matrix. Mathematically, we may model the 2D image estimate as

$$\hat{c}(x, y) = \langle \hat{c}_{y_0}(x)\,\delta(y_0 - y)\rangle_{y_0}.$$

The PSF of the estimated image is determined by the integral

$$\text{PSF}(\mathbf{x}_\perp) = \sqrt{\frac{2}{\pi}}\,k_c^2\,\text{sinc}\left(k_c\,y\right)\int_{-1}^{1}\sqrt{1-\tau^2}\,\text{sinc}\left(k_c\,y\sqrt{1-\tau^2}\right)\,e^{i\,k_c\,x\,\tau}\,d\tau,$$

where we have defined $\tau = t/T$. This PSF has no analytic solution, but it can be evaluated numerically. The OTF does have an analytic solution that may be written in the form

$$\text{OTF}(\mathbf{k}_\perp) = \frac{1}{4}\,\text{Re}\left\{\sqrt{1-\left(\frac{k_x}{k_c}\right)^2}\right\}\sum_{p=1}^{4} f_p(\mathbf{k}_\perp). \tag{17}$$

Here we have defined

$$f_1(\mathbf{k}_\perp) = \left[1+\sqrt{1-\left(\frac{k_x}{k_c}\right)^2}-\frac{k_y}{k_c}\right]\text{sign}\left(1+\sqrt{1-\left(\frac{k_x}{k_c}\right)^2}-\frac{k_y}{k_c}\right),$$

$$f_2(\mathbf{k}_\perp) = -\left[1-\sqrt{1-\left(\frac{k_x}{k_c}\right)^2}+\frac{k_y}{k_c}\right]\text{sign}\left(1-\sqrt{1-\left(\frac{k_x}{k_c}\right)^2}+\frac{k_y}{k_c}\right),$$

$$f_3(\mathbf{k}_\perp) = -\left[-1+\sqrt{1-\left(\frac{k_x}{k_c}\right)^2}+\frac{k_y}{k_c}\right]\text{sign}\left(-1+\sqrt{-1+\left(\frac{k_x}{k_c}\right)^2}+\frac{k_y}{k_c}\right),$$

and

$$f_4(\mathbf{k}_\perp) = \left[1 + \sqrt{1 - \left(\frac{k_x}{k_c}\right)^2} + \frac{k_y}{k_c}\right] \operatorname{sign}\left(1 + \sqrt{1 + \left(\frac{k_x}{k_c}\right)^2} + \frac{k_y}{k_c}\right).$$

The imaging resolution is asymmetric along the x and y directions. In addition, as resolution enhancements for CHIRPT and SPIFI only occur along the modulation direction, higher order terms ($q > 1$) that arise in super resolution SFP imaging [25] further exacerbate this resolution anisotropy. In the tomography section, we discuss methods to eliminate this anisotropy in the imaging resolution and to expand super resolution along all imaging directions.

For second order SPIFI line scan imaging, we again find that this PSF has no analytic solution and is given by the integral

$$\mathrm{PSF}(\mathbf{x}_\perp) = \frac{3}{4}\int_{-1}^{1} \left(1-\tau^2\right)^2 \operatorname{sinc}^2\left(k_c\, y\, \sqrt{1-\tau^2}\right) e^{i\,2\,k_c\,x\,\tau}\, d\tau.$$

This integral is readily evaluated numerically.

The OTF does have an analytic solution that may be written in the form

$$\mathrm{OTF}(\mathbf{k}_\perp) = \frac{1}{4}\sum_{p=1}^{5} g_p(\mathbf{k}_\perp). \tag{18}$$

Here we have defined

$$g_1(\mathbf{k}_\perp) = k_y \operatorname{sign}\left(k_y - 2\,k_c\sqrt{1-\left(\frac{k_x}{2\,k_c}\right)^2}\right),$$

$$g_2(\mathbf{k}_\perp) = k_y \operatorname{sign}\left(k_y + 2\,k_c\sqrt{1-\left(\frac{k_x}{2\,k_c}\right)^2}\right),$$

$$g_3(\mathbf{k}_\perp) = -2\,k_y \operatorname{sign}\left(k_y\right),$$

$$g_4(\mathbf{k}_\perp) = 2\,k_c\sqrt{1-\left(\frac{k_x}{2\,k_c}\right)^2} \operatorname{sign}\left(k_y + 2\,k_c\sqrt{1-\left(\frac{k_x}{2\,k_c}\right)^2}\right),$$

and

$$g_5(\mathbf{k}_\perp) = -2\,k_c\sqrt{1-\left(\frac{k_x}{2\,k_c}\right)^2} \operatorname{sign}\left(k_y - 2\,k_c\sqrt{1-\left(\frac{k_x}{2\,k_c}\right)^2}\right).$$

The asymmetry of 2D OTF is shown in Fig. 13. Panel (a) shows the first order OTF support, with the coherent cutoff of the x spatial frequency shown left-to-right, and the autocorrelation of the y coherent spatial frequency support evident along the y spatial frequency direction; spatial images simulated with this anisotropic spatial frequency support are shown in (b). Panel (c) shows the OTF for second order SPIFI. Along the x spatial frequency direction, the convex spatial frequency support shown in the 1D cross section of Fig. 3 is evident, whereas along the y direction, we still have the concave spatial frequency support from the focused beam; spatial images simulated with this anisotropic spatial frequency support are shown in (d).

3.2.2. Two-dimensional axial CHIRPT imaging: single pixel fluorescent holography

In this section, we describe the remarkable ability of the sparse spatial frequency projection (SFP) imaging to mimic coherent optical scattering when detecting fluorescent light. This capability is surprising given that fluorescent light is emitted by molecules or atoms in an excited state with an excited state lifetime orders of magnitude shorter than temporal response time of any optical detector. Moreover, the random relative phase of each fluorophore makes such emission spatially incoherent. Under normal circumstances in incoherent imaging, such as fluorescent microscopy, the spatial incoherence of the emission means that all spatial phase information is lost from the recorded signal because each fluorescent molecule emits light with phase fluctuations uncorrelated with any other fluorescent molecule. The physical implication of the spatially incoherent light emission is that the emitted light direction is isotopic because the random phase fluctuations average over all propagation directions.

The net result of the incoherence of the emitted fluorescent light is that the fluorescent light propagation direction bears no relationship to the direction of input light, i.e., the illumination beam. The loss of the relationship between the fluorescent light and the illumination light is rather unfortunate because the incoherent light emission cannot be used for inverse scattering or holography under normal circumstances. While the self-interference of individual fluorescent emitters can be used in an imaging system to encode depth information by imparting an intensity pattern that changes with the fluorescent emitter location [57,58]; these strategies come at the cost of a loss of photon power by the need to pass through a diffractive optical element.

We have developed a method that is able to mimic coherent optical scattering by performing fluorescent holographic imaging by transferring the phase difference of two illumination beams onto a time-dependent modulation of fluorescent emission intensity [21,53]. Such single pixel fluorescent holographic imaging is possible because the kernel for the forward operator in CHIRPT is produced by interference between two incident waves. This enables the stable phase evolution accumulated by the coherent illumination beam to be transferred from the spatially coherent illumination to a time-varying emission of the fluorescent emission intensity in an imaging mode called Coherent Holographic Image Reconstruction by Phase Transfer (CHIRPT) [21]. This unique capability allows CHIRPT imaging to perform coherent imaging with incoherent (e.g., fluorescent) light, such as fluorescent holography [21].

In single pixel fluorescent CHIRPT holography, we consider illumination of an object (with a thin, uniform illumination in height along y), so that we reduce our system to a 2D axial CHIRPT imaging problem. Here, we may consider our general CHIRPT kernel function evaluated at $y = 0$. The kernel for the forward operator is then

$$\Psi^{\mathrm{CH2DA}}(\mathbf{x}_\parallel, t) = e^{-i\,\Delta k_x(t)\,x}\, e^{-i\,\Delta k_z(t)\,z}, \tag{19}$$

where $\mathbf{x}_\parallel = (x, z)$. Much like in holographic imaging with coherently scattered light, we can extract axial information from a single time-trace measurement by inverting the forward operator, which is given by

$$\mathcal{D}\{c(\mathbf{x}_\parallel)\}(t,\phi) = \left\langle \beta(t)\, \Psi^{\mathrm{CH2DA}}(\mathbf{x}_\parallel, t)\, c(\mathbf{x}_\parallel)\right\rangle_{\mathbf{x}_\parallel}. \tag{20}$$

No closed form dual kernel has been found for CHIRPT. However, we can analyze the use of the adjoint of the kernel of the forward operator to estimate the object. Unfortunately, the adjoint and the forward kernels fail to establish a biorthogonal relationship, and consequentially CHIRPT fluorescent holography fails to achieve axial sectioning, just as is the case with coherent linear scattering.

Using the adjoint for reconstruction allows for the collected fluorescent light power to be reconstructed in a manner that is exactly analogous to coherent holographic imaging, but using incoherent light emission. The PSF for 2D axial CHIRPT is

$$\mathrm{PSF}(\mathbf{x}_\parallel) = \frac{2}{\pi}\int_{-1}^{1} \sqrt{1-\tau^2}\, e^{-i\,k_c\,x\,\tau}\, e^{-i\,k\,z\,(\sqrt{1-(\mathrm{NA_{ill}}\,\tau)^2}-1)}\, d\tau. \tag{21}$$

The OTF for this imaging modality is obtained by direct Fourier transform and reads

$$\mathrm{OTF}(\mathbf{k}_\parallel) = \mathrm{Re}\left\{\sqrt{1-\left(\frac{k_x}{k_c}\right)^2}\right\} \delta\left[k_z - k\left(\sqrt{1-\left(\frac{k_x}{k}\right)^2} - 1\right)\right]. \tag{22}$$

Note that the OTF is identical to the Fourier Diffraction Theorem shown by Wolf when analyzing coherent holographic imaging [59].

4. Spatial frequency projection tomographic imaging

As noted above and shown in Fig. 13, the spatial resolution in the plane transverse to the optic axis is anisotropic as a result of differences in image formation along and perpendicular to the modulation direction (x in our model). Single-pixel tomographic imaging strategies were developed for homogenizing the spatial resolution along the transverse spatial coordinates that are based on a relative rotation through an angle ϕ, as shown in Fig. 2, about the optical axis of the illumination beam and a thin planar object [33,48,49]. Consequentially, these tomographic imaging methods require a relative rotation between the illumination light and the object.

The forward operator for a rotated illumination can be expressed as

$$\tilde{\boldsymbol{\Phi}}_0(t,\phi) = D\{c(\mathbf{x}_\perp)\}(t,\phi) = \langle \beta(t)\, \Psi_\phi(\mathbf{R}_\phi\, \mathbf{x}_\perp, z_0, t)\, c(\mathbf{x}_\perp)\rangle_{\mathbf{x}_\perp}, \tag{23}$$

where $\mathbf{R}_\phi$ that produces a transformation of the transverse plane that leads to $\mathbf{x}_\perp = (x,y) \rightarrow \mathbf{R}_\phi\, \mathbf{x}_\perp = (x\cos\phi - y\sin\phi, x\sin\phi + y\cos\phi)$ and $\beta(t) = \mu(t)$. The Fourier kernel of the forward operator for transverse SFP tomography is

$$\Psi_\phi^{\mathrm{TT}}(\mathbf{x}_\perp, z_0, t) = \rho_{0,1}(\mathbf{R}_\phi\, y, z_0)\, e^{i\, \boldsymbol{\Delta}\mathbf{k}_\perp(t)\cdot \mathbf{R}_\phi\, \mathbf{x}_\perp}\, e^{i\, \Delta k_z(t)\, z_0}. \tag{24}$$

The inverse operator depends on assumptions made in the intensity envelope along the y direction, Fig. 7 column (a). When we have a limiting case of a uniform beam, where $\rho_{0,1}(y) \rightarrow 1$, then we have the case of Lateral Tomography (LT) [48]. LT mathematically conforms to standard parallel ray computed tomography [60]. In the alternate limiting case of a very tight line focus, where $\rho_{0,1}(y) \rightarrow \delta(y)$, then we obtain a conjugate domain version of computed tomography called Fourier Computed Tomography (FCT) [49]. However, any realistic experiment has a finite spatial support in $\rho_{0,1}(y)$ that conforms to neither of the limiting cases, which we also investigate in this review.

4.1. Lateral SFP tomography

Lateral tomography [48] assumes a uniform illumination across the transverse spatial extent of the object, schematic drawing Fig. 4 panel (1), so that

$$\Psi_\phi^{\mathrm{LT}}(\mathbf{x}_\perp, z_0, t) = e^{i\, \boldsymbol{\Delta}\mathbf{k}_\perp(t)\cdot \mathbf{R}_\phi\, \mathbf{x}_\perp}\, e^{i\, \Delta k_z(t)\, z_0}. \tag{25}$$

The inverse operator is readily obtained by constructing the object estimate from in inverse Fourier transform, with the inverse operator

$$\hat{c}_0(\mathbf{x}_\perp) = D_{\mathrm{LT}}^{-1}\{\tilde{\boldsymbol{\Phi}}_0(t,\phi)\}(\mathbf{x}_\perp) = \langle \tilde{\Psi}^{\mathrm{LT},\dagger}(x,t)\, \tilde{\boldsymbol{\Phi}}_\phi(t)\rangle_{(t,\phi)}. \tag{26}$$

The dual kernel, $\tilde{\Psi}^{\mathrm{LT},\dagger}(x,t)$, of the inverse operator is weighted by the magnitude of the determinate of Jacobian for the coordinate transformation through a rotation angle ϕ. This leads to $\tilde{\Psi}^{\mathrm{LT}}(\mathbf{x}_\perp, t) = |t|\, \Psi^{\mathrm{LT}}(\mathbf{x}_\perp, t)$. The dual kernel satisfies the biorthogonality condition in the limit of large NA. The imaging resolution and frequency support are azimuthally uniform, and are expressed as

$$\mathrm{PSF}(\|\mathbf{x}_\perp\|_2) = \frac{3}{k_c^3}\, \frac{\sin(k_c\|\mathbf{x}_\perp\|_2) - k_c\, \|\mathbf{x}_\perp\|_2\, \cos(k_c\, \|\mathbf{x}_\perp\|_2)}{\|\mathbf{x}_\perp\|_2^3} \tag{27}$$

and

$$\mathrm{OTF}(\|\mathbf{k}_\perp\|_2) = \mathrm{Re}\left\{\sqrt{1 - \left(\frac{\|\mathbf{k}_\perp\|_2}{k_c}\right)^2}\right\}. \tag{28}$$

LT produces images in a 2D plane orthogonal to the direction of propagation. The tomographic imaging homogenizes the transverse spatial frequency support, making the OTF azimuthally symmetric in transverse x-y spatial frequency plane. The radial PSF and OTF cross sections are shown in Fig. 5, with the first order indicated by the blue line.

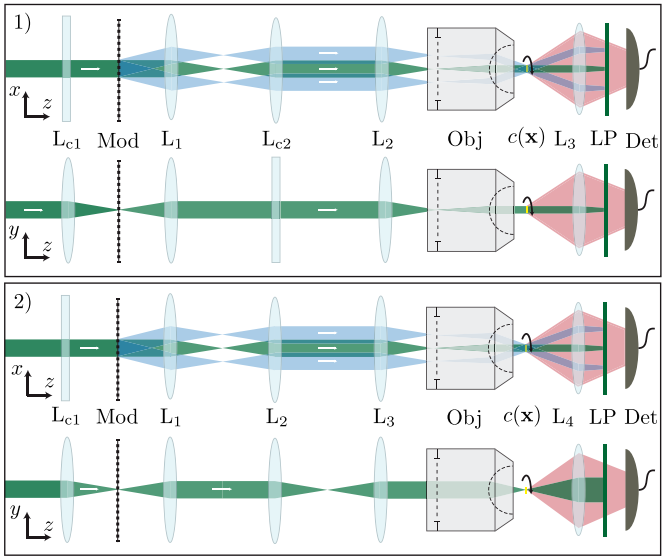

Fig. 4. Schematic diagram of Lateral Tomography (LT) and Fourier Computed Tomography (FCT). Panel (1) shows the schematic drawing of an LT microscope. Due to the asymmetry of the illumination both the xy and yz views are shown top and bottom, respectively. Panel (2) shows the schematic drawing of a FCT microscope, note the difference in illumination at the sample plane. $L_{c1,2}$ — Cylindrical Lens, L_{1-4} — Spherical Lens, *Mod* — Modulator, *Obj* — Objective Lens, $c(\mathbf{x})$ — Sample, *LP* — Long Pass Filter, *Det* — Detector.

In the case of second order SPIFI lateral tomography, the PSF then reads

$$\mathrm{PSF}(\|\mathbf{x}_\perp\|_2) = \frac{J_2\left(2\, k_c\, \|\mathbf{x}_\perp\|_2\right)}{k_c^2\, \|\mathbf{x}_\perp\|_2^2}, \tag{29}$$

and the OTF is

$$\mathrm{OTF}(\|\mathbf{k}_\perp\|_2) = \left(\mathrm{Re}\left\{\sqrt{1 - \left(\frac{\|\mathbf{k}_\perp\|_2}{2\, k_c}\right)^2}\right\}\right)^2. \tag{30}$$

Fig. 5 shows the first (blue), second (green), third (orange), and fourth (purple) order PSF of lateral tomography (left) and the corresponding OTF (right). We see that the resolution increases as the image order increases. Note the convex shape of the OTF of the 3rd and 4th orders which have high amplitude support at the highest spatial frequencies providing very good imaging performance.

Second order LT imaging also produces an azimuthally symmetric PSF and OTF with double the transverse spatial frequency support of the first order SPIFI case. Higher orders are also shown in Fig. 5, illustrating that the improved spatial frequency support from higher order SFP orders can be extended to isotropic super-resolution imaging. However, even the second order imaging is improved compared to simple wide-field imaging that displays the same cutoff spatial frequency, at $2\, k_c$. In the case of second order SFP tomography, the convex spatial frequency support produces images that are superior to those obtained with widefield incoherent imaging even though the cutoff spatial frequency is identical. This point is shown in Fig. 14 and the ability of SFP tomography improve image quality based on the more favorable spatial frequency support is elaborated in the discussion section.

4.2. Fourier SFP tomography

Fourier computed tomography (FCT) [49] uses a tightly focused line illumination that is approximated as a delta function along the y

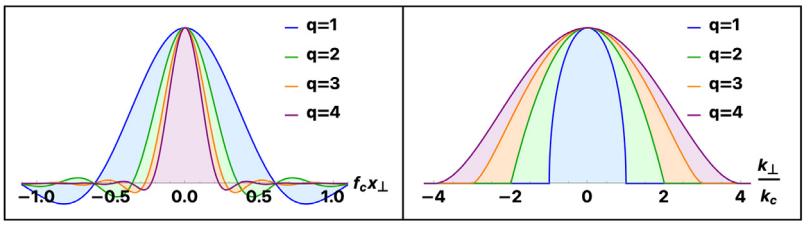

Fig. 5. Plots of the SPIFI LT PSF (left) and OTF (right) up to fourth order. The spatial frequency support is isotropic in the lateral spatial frequency plane, and thus the plot if over the transverse axial spatial frequency support. The axes are normalized in terms coherent cutoff spatial frequency, $k_c = 2\pi f_c$.

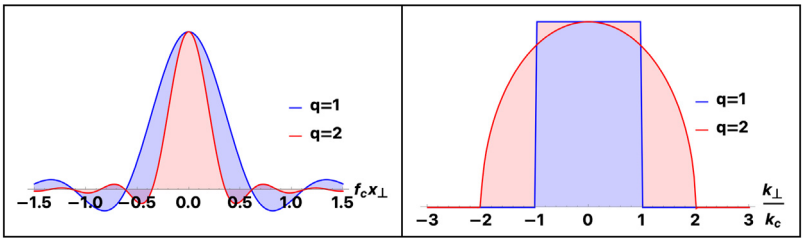

Fig. 6. (left) A plot of the first and second order FCT PSF. (right) A plot of the first and second order FCT OTF. The axes are normalized in terms of coherent cutoff spatial frequency, $k_c = 2\pi f_c$.

direction, as shown schematically drawing Fig. 4 panel 2). In the focal plane, where $z_0 = 0$, the Fourier kernel of the forward operator reads

$$\Psi_\phi^{\mathrm{FCT}}(\mathbf{x}_\perp, z_0, t) = \delta(\mathbf{R}_\phi \mathbf{y}_\perp)\, e^{i\, \Delta\mathbf{k}_\perp(t)\cdot \mathbf{R}_\phi \mathbf{x}_\perp}. \tag{31}$$

Here we have defined the perpendicular y-vector as $\mathbf{y}_\perp = (0, y)$. The forward operator produces the time-domain signal

$$\Phi(t,\phi) = \mathcal{D}\{c(\mathbf{x}_\perp)\}(t,\phi) = \langle \beta(t)\, \Psi_\phi^{\mathrm{FCT}}(\mathbf{x}_\perp, z_0, t)\, c(\mathbf{x}_\perp)\rangle_{\mathbf{x}_\perp}. \tag{32}$$

The temporal signal collects information from the object as a sequence of spatial frequency projections, but we wish to estimate the images using the spatial slice theorem, we transform the acquired data to the temporal frequency domain,

$$\check{\Phi}(\nu,\phi) = \mathcal{F}_t\{\Phi(t,\phi)\}(\nu) = \int \Phi(t,\phi)\, \exp(-i\, 2\pi\, \nu\, t) dt.$$

By further expanding the object distribution in terms of transverse spatial frequency vectors

$$c(\mathbf{x}_\perp) = \mathcal{F}^{-1}\{C(\mathbf{k}_\perp)\},$$

we obtain the FCT forward model given by

$$\check{\Phi}(\nu,\phi) = \mathcal{D}\{C(\mathbf{k}_\perp)\}(\nu,\phi) = B(\nu) * \langle \check{\Psi}_\phi^{\mathrm{FCT}}(\mathbf{x}_\perp, 0, \nu)\, C(\mathbf{k}_\perp)\rangle_{\mathbf{k}_\perp}. \tag{33}$$

Here the forward FCT operator, $\check{\Psi}_\phi^{\mathrm{FCT}}(\mathbf{x}_\perp, 0, \nu) = (2\pi/\gamma)\, \exp(-i\, 2\pi\, (\nu/\gamma)\, \mathbf{R}_\phi\, \mathbf{k}_\perp)$, acts on the object spatial frequency distribution $C(\mathbf{k}_\perp) = \mathcal{F}\{c(\mathbf{x}_\perp)\}$, forming a complex Radon transform in the spatial frequency domain. The spatial frequency projections are convolved with the spectrum of the weighing function, $B(\nu) = \mathcal{F}\{\beta(t)\}$, where $*$ is the convolution operator with respect to ν.

The inverse operator is readily obtained by constructing the object estimate from in inverse Fourier transform and applying the magnitude of the determinant of the Jacobian coordinate transform, leading to

$$\hat{C}(\mathbf{k}_\perp) = \mathcal{D}_{\mathrm{FCT}}^{-1}\{\check{\Phi}(\nu,\phi)\}(\mathbf{k}_\perp) = \langle \check{\Psi}^{\mathrm{FCT},\dagger}(\mathbf{k}_\perp, \nu)\, \check{\Phi}(\nu,\phi)\rangle_{(\nu,\phi)}. \tag{34}$$

The dual kernel of the inverse operator is weighted by the magnitude of the Jacobean from the coordinate transform, leading to $\check{\Psi}^{\mathrm{FCT}}(\mathbf{k}_\perp, \nu) = |\nu|\, \check{\Psi}_\phi^{\mathrm{FCT}}(\mathbf{x}_\perp, 0, \nu)$. Support extends to the coherent cutoff spatial frequency.

In the case of first-order SPIFI FCT, the PSF evaluates to

$$\mathrm{PSF}(\|\mathbf{x}_\perp\|_2) = \frac{2\, J_1\left(k_c\, \|\mathbf{x}_\perp\|_2\right)}{k_c\, \|\mathbf{x}_\perp\|_2}, \tag{35}$$

and the OTF is

$$\mathrm{OTF}(\|\mathbf{k}_\perp\|_2) = \mathrm{rect}\left(\frac{\|\mathbf{k}_\perp\|_2}{2\, k_c}\right). \tag{36}$$

For second-order SPIFI FCT, the PSF is

$$\mathrm{PSF}(\|\mathbf{x}_\perp\|_2) = \frac{3}{8}\, \frac{\sin(2\, k_c\, \|\mathbf{x}_\perp\|_2) - 2\, k_c\, \|\mathbf{x}_\perp\|_2\, \cos(2\, k_c\, \|\mathbf{x}_\perp\|_2)}{(k_c\, \|\mathbf{x}_\perp\|_2)^3}, \tag{37}$$

and the OTF is

$$\mathrm{OTF}(\|\mathbf{k}_\perp\|_2) = \frac{1}{2\, k_c} \int_0^\infty \frac{\sin(2\, k_c\, \rho) - 2\, k_c\, \rho\, \cos(2\, k_c\, \rho)}{\rho^2}\, J_0(\|\mathbf{k}_\perp\|_2\, \rho)\, d\rho. \tag{38}$$

Fig. 6 shows the PFS and OTF for FCT for the first and second order images.

4.3. Generalized transverse SFP tomography

For the generalized transverse SFP tomography (GTT) problem, the projected illumination pattern height along the y-direction appears with a thickness between that of LT and FCT. Indeed, LT and FCT are limiting cases of the generalized problem of a beam with an arbitrary width. In the case of LT, a uniform illumination is assumed across the entire object transverse width. Alternately, in the FCT limit, the illumination is assumed to be an infinitesimally thin line.

Under many experimental conditions, where an illumination line of a finite width is used, the reconstruction methods for the LT and FCT modalities are not sufficient to produce accurate results as the assumptions made in each do not apply for the generalized problem. Fig. 7 summarizes this point. That is, row (1) panel (1a) illustrates the illumination pattern for LT, panel (1b) shows the probed spatial frequency at a snap shot in time, (1c) shows the sinogram generated from a 180 degree rotation of the illumination beam. Since the illumination beam (1a) is uniform along y_ϕ, the object will be illuminated at all rotation angles, ϕ, therefore creating continuous arcs in the sinogram. Panel (1d) shows the image reconstruction of LT. Similarly, Fig. 7 row (3) shows similar information except for the FCT imaging modality. What is important to note is how the sinogram changes (3c). Instead of creating long continuous lines as in LT (1c) they are instead short narrow lines which start long near the center of rotation and get shorter further away. This is a result of the illumination being very narrow in y_ϕ. In the case of generalized transverse tomography (GTT), row

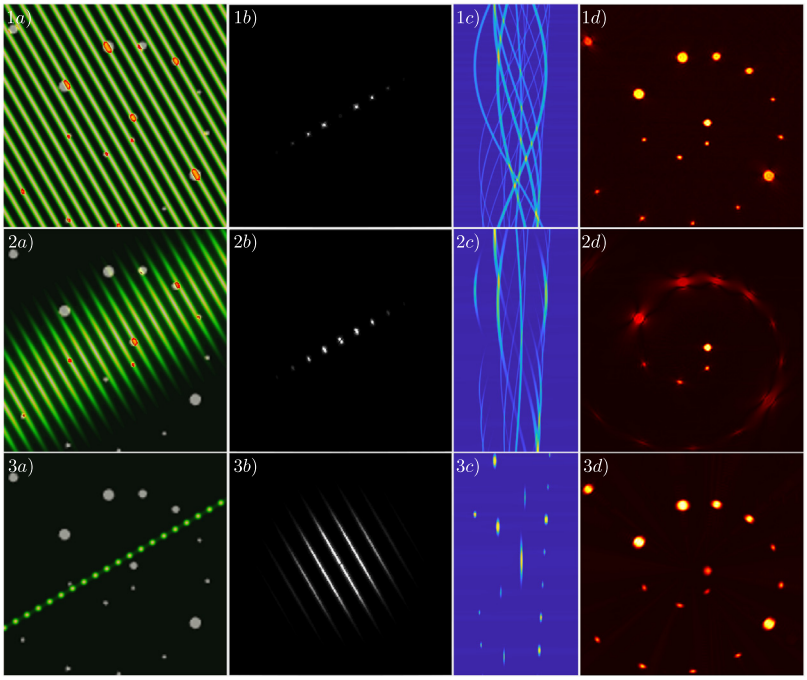

Fig. 7. Conceptual diagram of Lateral Tomography (LT), Generalized Transverse Tomography (GTT), and Fourier Computed Tomography (FCT). Row (1) shows LT work flow, row (2) shows GTT, and row (3) show FCT. Column (a) shows the illumination in the xy-plane for each modality. Column (b) shows the spatial frequencies probed by the illumination at an illumination angle and instantaneous spatial frequency. Column (c) shows the sinogram for each modality where the vertical axis is rotation angle and the horizontal axis is x_ϕ. Column (d) shows the object reconstruction for each modality. Panel (2d) was reconstructed using the algorithm for LT, we see that the reconstruction is severely distorted due to the fact that the illumination does not conform to the illumination assumptions made for LT.

(2), the illumination is somewhere between the two limiting cases of LT and FCT. This results in a sinogram, panel (2c), giving elongated discontinuous arcs. As a result neither reconstruction algorithm is well suited for provide a quality reconstruction. Panel (2D) shows the reconstruction of GTT using the LT reconstruction algorithm.

The forward kernel for GTT is given by

$$\Psi_\phi^{\mathrm{GTT}}(\mathbf{x}_\perp, z_0, t) = e^{-\left(\frac{\mathbf{R}_\phi vyp}{w_y}\right)^2} e^{i\,\Delta\mathbf{k}_\perp(t)\cdot\mathbf{R}_\phi\,\mathbf{x}_\perp}\, e^{i\,\Delta k_z(t)\,z_0}. \tag{39}$$

The case we consider here is described in Eq. (39) where the y spatial support has a finite width given by a Gaussian envelope $\rho_{0,1}(\mathbf{R}_\phi y, w_y) \rightarrow e^{-\left(\frac{\mathbf{R}_\phi vyp}{w_y}\right)^2}$. Where w_y defines the 1/e field width of the beam along the y direction.

To date, no analytic inverse operator has been found for this general problem. Instead, we can solve the problem as an open form optimization problem of the form given in Eq. (1). While this strategy avoids the need for finding an inverse operator, and we are able to relax the assumptions on the y spatial support in LT and FCT to allow a general illumination beam in the forward kernel function, $\Psi_\phi^{\mathrm{GTT}}(\mathbf{x}_\perp, z_0, t)$, the lack of an analytic inverse operator significantly increases computational complexity and cost for estimating the object.

To solve the general SFP transverse tomography problem, we frame it as an open form computational imaging problem. We employ an accurate physical model of the illumination pattern and its interaction with the sample. By sampling the continuous forward model, we convert the forward operator to a measurement matrix that acts on a discrete, vectorized object, $\mathbf{c}$. With the measurement matrix and appropriately formatted data, an accurate image can be formed by solving Eq. (1). There exists a wealth of knowledge in solving these types of optimization problems [43]. Many of these techniques produce very nice results with the added ability to define constraints on the solution using prior information. In some cases, this can drastically improve the SNR of the image in the presence of noise [44].

Using the model of the illumination intensity developed in the preceding sections, we can build a discrete measurement matrix for the generalized transverse SFP tomography problem. The construction of the measurement matrix is illustrated in Fig. 8. As the 2D object is converted into a 1D column vector represented by $\mathbf{c}$ that is labeled as the object in the figure, then each row of the measurement matrix is a 1D row vector samples of 2D forward kernel, $\Psi_\phi^{\mathrm{GTT}}(\mathbf{x}_\perp, z_0, t)$, for a sample particular angle and time. Here $\mathbf{x}_\perp$ is a 1D column vector assembled from the discrete 2D array of spatial point in the transverse plane. The full measurement matrix is a concatenation of measurement matrices for a single rotation angle, ϕ_p. The elements of the measurement matrix are then given by $[\mathbf{A}]_{i,j}^{\phi_p} = \Psi_\phi^{\mathrm{GTT}}([\mathbf{x}_\perp]_j, z_0, t_i)$. Each row of the measurement matrix is a flattened 2D discrete model of the illumination pattern, at a particular angle and time sample, as shown in the top row of Fig. 8. The entire set of time samples is assembled as groups of rows for each discrete angle ϕ_p, where p is an index that runs over the set of N_ϕ discrete measurement angles over the range $\phi = [0, \pi_{\max}]$, as illustrated in the figure.

In each angular block, the signal model for a time t_i is the inner product, between the ith row of $\mathbf{A}^{\phi_p}$ and the object column vector $\mathbf{c}$. Physically, this inner product represents a two-dimensional overlap integral between the SPIFI intensity distribution at the time t_i and the object. The signal model for this angle is $\mathbf{y}^{\phi_p} = \mathbf{A}^{\phi_p}\mathbf{c}$. The measured signal from each angle, $\mathbf{y}^{\phi_p}$, is concatenated to assemble the full signal column $\mathbf{y} = (\mathbf{y}^{\phi_1} \mid \mathbf{y}^{\phi_2} \mid \cdots \mid \mathbf{y}^{\phi_{N_\phi}})^T$ as is illustrated in the right hand side of Fig. 8. This form of the matrix ensures that the result of the operation of this matrix onto an object gives a set of photodiode signals stacked on top of one another in a vector. Fig. 8 illustrates the structure of the measurement matrix, object, and data (SPIFI sinogram).

Having formulated the measurement matrix, the computational imaging problem becomes the optimization problem expressed in Eq. (1). The general description of this optimization problem as applied to generalized transverse SFP tomography is shown schematically in Fig. 9. Simulations of the generalized transverse SFP tomography problem were carried out by solving the inverse problem as posed above using an algorithm called FISTA (Fast Iterative Shrinkage Thresholding Algorithm). The estimated image vector returned by the optimization algorithm can be reformatted into a 2D image.

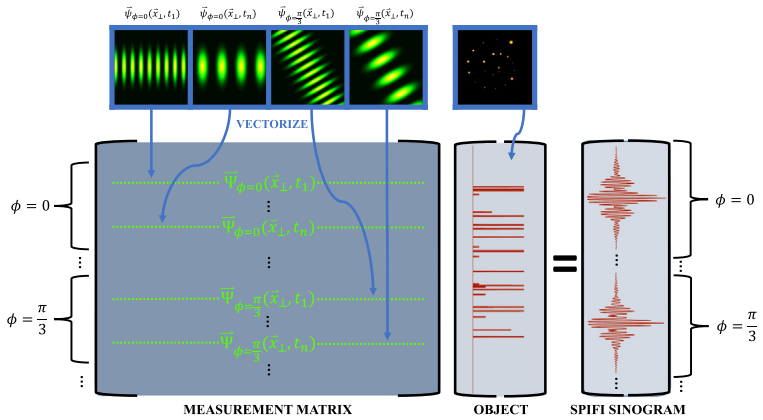

Fig. 8. Illustration of how the measurement matrix construction and the signal model. The object is a discrete 2D object sampled over $N_x \times N_y$ points that has been flattened to a $1 \times N_x N_y$ column vector. The top row shows examples of the 2D illumination pattern for the pth rotational angle at time t_i. Each 2D illumination pattern is flattened into a row and stacked into a series of time samples running from $i \in \{1, \ldots, N_t\}$ for the pth angle. Each angle increment then has a new stack of flattened 2D illumination patterns that run over the sample times. Thus the measurement matrix contains $N_\phi \times N_t$ rows and $N_x \times N_y$ columns. The signal model is a stack of each measured time vector for each rotation angle.

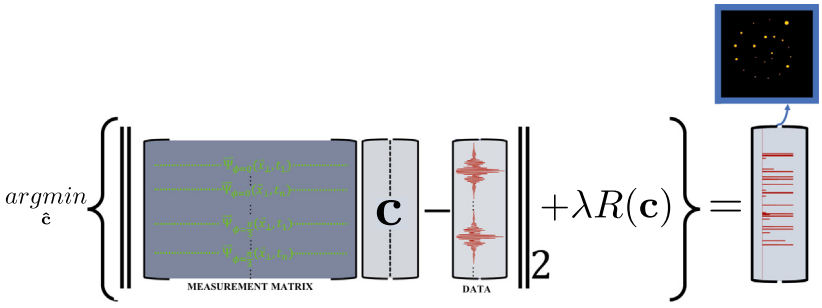

Fig. 9. Generalized transverse SFP tomography inverse problem with regularization.

Numerical simulation data was generated by computing SPIFI time traces at a set of discrete rotation angles and time steps that correspond to a particular illumination pattern for a 30 μm Gaussian line focus. The data are calculated on a spatial and temporal grid much finer than used in the model for reconstruction and then down-sampled to avoid inverse crimes [61,62]. The chosen beam size of 30 μm lies comfortably between the regimes of FCT and LT. Results of the simulation are shown in Fig. 10, along with comparisons of reconstructing the generalized problem using the FCT and LT analytic reconstruction algorithms.

Although the direct solution of the optimization problem produces image estimates of good quality, this strategy is hard to scale to large image sizes due to the computational burden for image estimation. The number of elements in the measurement matrix is $\text{size}(A) = [N_\phi N_t \times N_x N_y]$ where N_θ, N_t, N_x, and N_y are the number of discrete angular, time, x-axis bin, and y-bin samples, respectively, with each dimension having to be sampled appropriately. The size of this matrix becomes unmanageable very quickly. Especially when driving nonlinearities in the sample, the time dimension must have a large number of time points, on the order of 2^{12}. For a realistic problem size, the amount of memory required to instantiate the measurement matrix would be approximately 1.2 TB. This memory requirement is in excess of what most computers can handle.

A method to circumvent the need for instantiating large matrices into memory is to formulate the measurement matrix and its adjoint in terms of operators in functional form that require much lower memory requirements. The adjoint operation is required by many optimization algorithms, including the FISTA algorithm [63] in order to calculate the gradient of Eq. (1). Although recasting the large measurement matrix in the form of functional operators mitigates the memory storage bottleneck, the computational burden now lies in computational time, leading to much longer computer run times for image estimation. Using a computer with a 3.0 GHz processor, 4 cores, and 32 GB of RAM it would take about 6 days to run 150 iterations of FISTA to solve for a 256×256 image. For the simulation shown above, approximately 1500 iterations are required to reach a minimum in Eq. (1). The simulation results were obtained using a single node on the Asha computer cluster at Colorado State University. One node has 2 x Intel Xeon Gold 6148 CPU (3.7 GHz, 40 total cores) and 192 GB of RAM. Parallel computing was utilized due to the large number of cores available in the processors. Utilizing this computing power, 2000 iterations of FISTA with a 256×256 image completed in 41.4 h.

These difficulties encountered in scaling the computational imaging to higher dimensions and higher spatial resolution can be used to solve the generalized transverse SFP tomography problem, but this strategy is burdened by significant computational difficulties. This complication further motivates the formulation of an analytic solution to generalized transverse SFP tomography.

4.4. Fluorescent diffraction tomography

As we have seen, CHIRPT is able to mimic coherent optical holography with a single pixel fluorescent holographic microscope. Holographic imaging can be understood in the context of Born scattering [59] and holography allows for 3D numerical refocusing of light, which is possible with imaged fluorescent light in CHIRPT. However, holography is not able to fully resolve a 3D structure along the axial direction. In coherent imaging, this deficiency is rectified by diffraction tomography, where a set of holograms are recorded as the direction of illumination of incident coherent illumination plane wave is varied. By scanning over a sufficiently large set of incident illumination angles, it

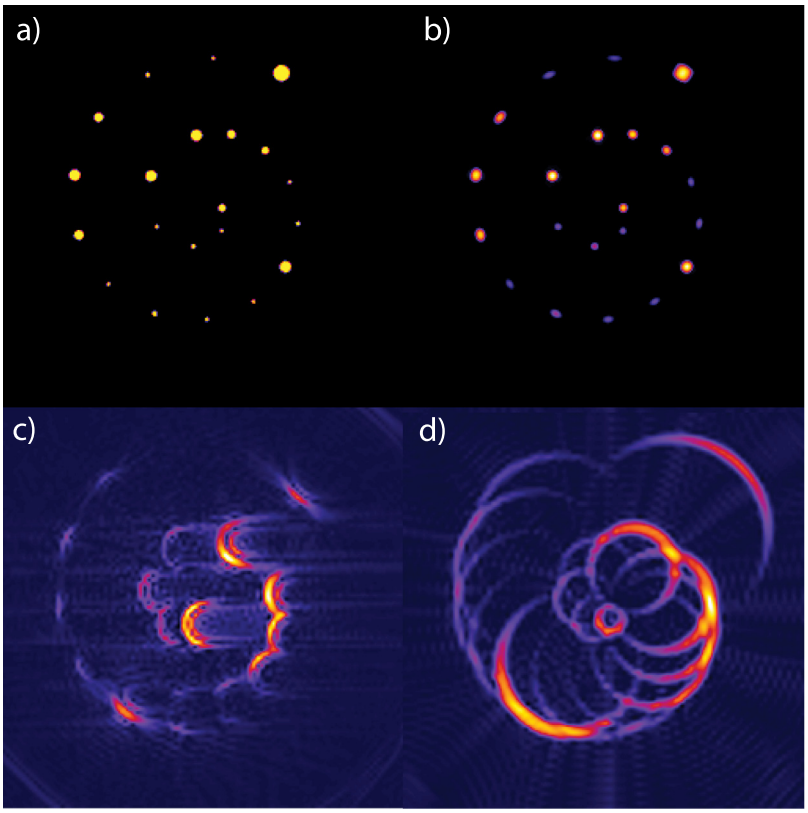

Fig. 10. (a) True object, (b) Generalized transverse tomography with FISTA, (c) Lateral tomography (d) Fourier computed tomography. Results of solving the generalized problem as a computational imaging problem using FISTA compared to attempting to reconstruct using FCT and LT methods with false assumptions.

is possible to solve the inverse scattering problem and provide detailed internal structure of a 3D object. Here, we demonstrate that single pixel fluorescent holographic imaging can be extended to enable diffraction tomographic imaging with incoherent light emission.

Single pixel fluorescent holography [21] using CHIRPT mimics coherent imaging, allowing for refocusing of the collected fluorescent signal to form a 2D image from a single measurement trace. A 3D image is created from a set of signals collected as the height of the line focused is scanned. Yet, detailed axial structure is elusive due to a lack of extended axial spatial frequency support that plagues holographic imaging [59]. Fluorescent diffraction tomography (FDT) [33] fills out the axial spatial frequency information through a relative rotation of the object about the y axis, with an polar angle, θ, with respect to the optical axis, z. We still assume that we illuminate a thin slice of an object along the y direction. In this case, the rotated single pixel fluorescent holography kernel that is given by

$$\Psi_{\theta}^{\mathrm{FDT}}(\mathbf{x}_{\parallel}, t) = \Psi^{\mathrm{CH2DA}}(\mathbf{R}_{\theta}\,\mathbf{x}_{\parallel}, t), \tag{40}$$

where $\mathbf{R}_{\theta}\,\mathbf{x}_{\parallel} = (x, z)$. The FDT data is now composed of a set of time traces taken at the relative polar angles, θ. The dual kernel of the inverse operator for FDT is given by $\tilde{\Psi}_{\theta}^{\mathrm{FDT}}(\mathbf{x}_{\parallel}, t) = \Gamma(t)\,\Psi_{\theta}^{\mathrm{FDT}}(\mathbf{x}_{\parallel}, t)$, where $\Gamma(t) = |t|/T\sqrt{1-(\mathrm{NA}\,t/T)^2}$. The inverse operator follows the familiar form given in Eq. (3). Unlike with single pixel fluorescent holography, the dual kernel now produces a biorthogonal pair in the limit as NA $\to \infty$. With the fringe visibility weighting functions, the PSF no longer has an analytic result, but the PSF is still well approximated by the biorthogonal function.

Due a lack of an analytic solution, the PSF in FDT remains in integral form as

$$\mathrm{PSF}(\mathbf{x}_{\parallel}) = \int_0^{\Delta\kappa_c} J_0\left(k\,\Delta\kappa\,\|\mathbf{x}_{\parallel}\|_2\right)\,\sqrt{\left(1-\frac{1}{2}\,\Delta\kappa^2\right)^2 + \mathrm{NA}_{\mathrm{ill}}^2 - 1}\;d\Delta\kappa,$$

where $\Delta\kappa_c^2 = 2 - 2\sqrt{1-\mathrm{NA}_{\mathrm{ill}}^2}$. Conversely the OTF has an analytic expression given by

$$\mathrm{OTF}(\|\mathbf{k}_{\parallel}\|_2) = \mathrm{rect}\left(\frac{\|\mathbf{k}_{\parallel}\|_2}{2\,k_{a,c}}\right)\,\mathrm{Re}\left\{\sqrt{\left(1-\frac{1}{2}\left[\frac{\|\mathbf{k}_{\parallel}\|_2}{k}\right]^2\right)^2 + \mathrm{NA}_{\mathrm{ill}}^2 - 1}\right\}.$$

The axial spatial frequency cutoff for FDT is defined as $k_{a,c} = k\,\Delta\kappa_c$ and $\mathbf{k}_{\parallel} = (k_x, k_z)$ is the spatial frequency vector that lies in the x–z plane. Note that the spatial frequency support is increased (by a factor of $\sqrt{2}$) as compared to the coherent cutoff spatial frequency. Line outs of the PSF and OTF along the x and z direction for FDT are shown in Fig. 11. Note that they are symmetric.

5. Aberrations in single pixel SFP tomography

Aberrations arise in optical systems when the optical path length through the imaging becomes dependent on the transverse spatial frequency as a result of a non-ideal optical imaging system. Under most circumstances, the aberrations are modeled as phase distortions applied to the coherent transfer function, $\mathcal{H}(\mathbf{k}_{\perp})$, which then produces a distortion in the radiant field of the beam envelope, $U_j(\mathbf{k}_{\perp})$.

As noted in a previous section, CHIRPT encodes the accumulated difference in spatial phase between the undiffracted and diffracted beams. This phase difference produces temporal modulations of light intensity emitted by each fluorophore. Consequently, individual fluorophores act as guide stars, reporting the total phase difference accumulated between the two beams from the modulation disk to the location of the fluorescent molecule. One of the great advantages of CHIRPT is the ability to remove aberrations in post-processing since the aberration phase is encoded directly into the measured signal [53]. Indeed, holographic projections are one form of aberration removal — specifically, removing propagation phase and/or adding more to form a full 2D image in the (x, z) plane. Deviations from the propagation

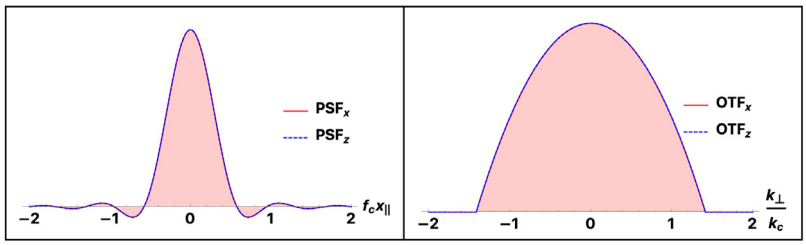

Fig. 11. The left panel shows the 2nd order x and z PSF for FDT. The right panel shows the corresponding frequency support, OTF, for the x and z directions. The axes are normalized in terms of coherent cutoff spatial frequency, $k_c = 2\pi f_c$. Note the resolution is isotropic.

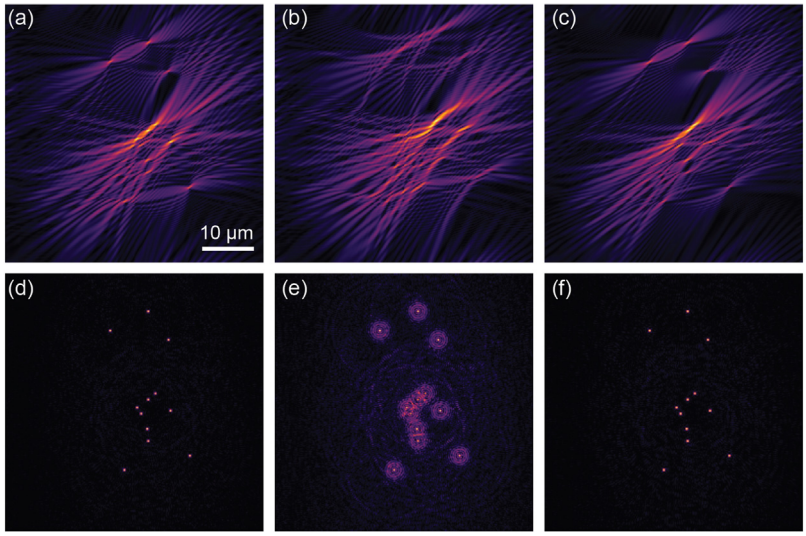

Fig. 12. Impact of index mismatch on FDT-CHIRPT. Reconstructions with a single illumination angle under (a) ideal imaging conditions, i.e., aberration free; (b) index mismatch between the immersion medium ($n = 1$) and the object medium ($n = 1.33$, water) where the medium of the object is not accounted for; and (c) index mismatch with the correct wavenumber included in the reconstruction. Tomographic reconstructions with 72 projection angles are shown for (d) ideal imaging, (e) mismatched index, and (f) mismatched index accounted for in the reconstruction.

phase dictated by the dispersion relation arising from solutions to the Helmholtz equation are also encoded and can be recovered and removed in the image estimation process in a variety of ways.

To explore the impact of aberrations in tomographic reconstructions in CHIRPT imaging, we consider the specific case of FDT-CHIRPT with a refractive index mismatch between the immersion medium and the object medium. More precisely, we consider an air-immersion 100x/0.9 NA objective lens and assume the specimen consists of a standard glass cover slip followed by water. We numerically simulated tomographic images for three cases: (1) ideal imaging, in which there is no index mismatch, (2) reconstruction of the images without accounting for the index mismatch, and (3) reconstruction of the images using the correct index for the object medium (water). The object is modeled as a distribution of Dirac-δ functions to represent individual fluorophores, which are arranged in the (x, z) plane at $y = 0$. For recognizably, we chose to arrange the emitters in the shape of the constellation Orion.

Fig. 12 shows the images simulated under all three conditions. In Fig. 12(a)–12(c), we show the holographic propagation using the forward model described above for CHIRPT with a projection angle of 30-deg. In Fig. 12(d)–12(f), we simulated images for 72 equally spaced viewing angles. The leftmost column shows the ideal case for CHIRPT, i.e., when no aberrations are present.

The figures in the middle column of Fig. 12 were computed by performing the reconstruction and assuming the local index of refraction matched that of the immersion medium. Note that while the set of spatial frequencies sampled in each of these two cases is identical, the resulting images are drastically different. To correct for this issue, one needs only to take into account the local index of refraction in the object when performing the reconstruction. The results of doing so are shown in the rightmost column where it is clear that the impact of the index change is to improve the quality of the resulting images.

Notably, the local index of refraction in the object is not always known *a priori* as it was in the simulation. In such cases, any guide-star within the object can be exploited to determine the average index of refraction in the sample using a computational inversion where the forward model incorporates an additional pupil phase term.

We note also that the introduction of aberrations can be beneficial, as we have shown in the case of accelerating light sheets that can be used to produce a uniform thickness imaging thickness along y for an extended distance in the axial direction, effectively mitigating the resolution degradation from diffraction of the light sheet [55].

6. Discussion

Single pixel imaging with structured illumination light is a powerful approach for optical imaging. Here we have reviewed several such strategies based on object illumination by a spatially coherent optical field that contains a sparse set of transverse spatial frequencies. The use of a small number of modulation spatial frequencies provides the ability to integrate many imaging modalities and multiplex information into an imaging platform. The use of sparse spatial frequencies confers a number of unconventional properties on SFP imaging. These unique properties include the ability to access a large field of view that is produced by a spatial frequency illumination with a compact spatial frequency support, while scanning through the full span of the transverse spatial frequency support of the objective. This is the origin of the improved image quality for SFP single pixel imaging discussed below. Image quality is improved due to the direct recording

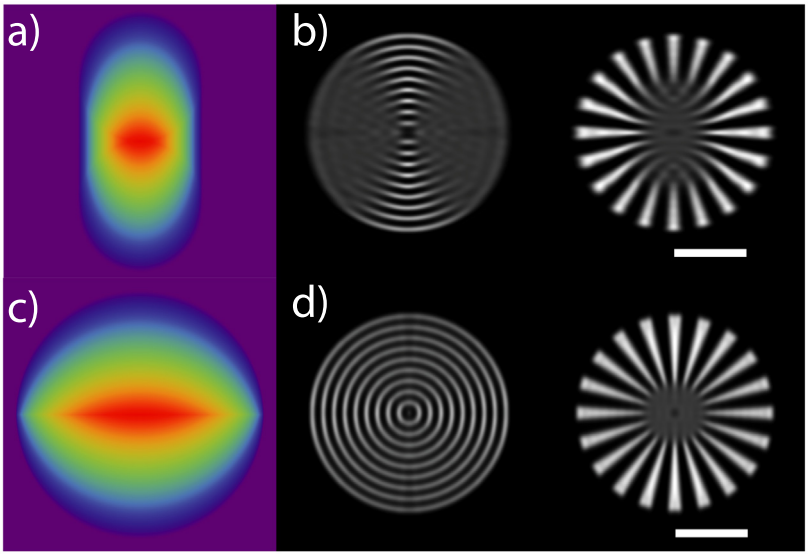

Fig. 13. The anisotropic imaging properties of line scan first and second order SPIFI are compared. (a) The OTF for line scanning 2D first-order SPIFI. (b) The simulated image for first order line scanning SPIFI. (c) The OTF for line scanning 2D second-order SPIFI. (d) The simulated image for second-order line scanning SPIFI. Note that along the modulation direction, i.e., the x-direction, the image is better resolved than along the scan direction (y-direction) even though the frequency cutoff is the same in both directions. The scale bar is 10 μm.

of aberrations, and that information can be exploited during image reconstruction for improved reconstructed image quality. This imaging modality can retain image fidelity when imaging through scattering media well beyond the transport mean free path length [52].

6.1. SFP imaging with a single pixel provides improved image quality

While it is conventional to characterize the quality of images produced in a microscope system by a single parameter, either the spatial resolution, δx, or the cutoff spatial frequency support, k_c, the use of a simple metric to quantify image quality fails to capture the full image quality and the ability to resolve structures in an object. In SFP imaging, the compact region of the illumination CTF used by any time-instance of the modulated illumination field means that single pixel SFP imaging transfer function (OTF) can deviate significantly from either the illumination or collection transfer functions. These differences also lead to improved shapes in the SFP imaging impulse response (PSF). Generally, the modulation transfer function (MTF = |OTF|, or the magnitude of the OTF) for SFP has a convex shape with respect to transverse spatial frequency distribution (see Fig. 14). By contrast, conventional imaging systems generally exhibit a concave MTF. The difference in the spatial frequency support has a stark impact on image quality. Note that even slight improvements in the MTF profile have generated significant excitement for pixel reassignment confocal microscopy techniques [64–67], where a slight improvement in mid-band transverse spatial frequencies lead to much better images. SFP imaging produces even more striking improvements.

Another way in which image quality is degraded is from aberrations that are introduced by imperfect imaging. In conventional imaging systems, a broad band of transverse spatial frequencies are either focused or collected to form images. As the imaging system sums over this broad range of transverse spatial frequencies, it is exceedingly challenging to back out the contributions to image degradation from the mix of aberration types that appear in normal imaging systems. In SFP imaging, the fact that a small subset of the transverse spatial frequency support (i.e., the CTF) of the illumination system is used for any instantaneous illumination field, aberration information is directly encoded as a phase modulation of the time-dependent signal. This phase modulation can be directly extracted and corrected in these systems.

Images and 2D transverse OTFs for non-tomographic line scanning are shown in Fig. 13. Both first and second order SPIFI are displayed in this figure. In both cases, the OTF support is anisotropic in lateral spatial frequencies. In first order SPIFI, we only span spatial frequencies up to the coherent spatial frequency cutoff along the modulation direction, but along the k_y direction the spatial frequency support is derived from the intensity of the illumination line height. In second order SPIFI, the cutoff spatial frequency is the same along both the k_x and k_y directions, yet image quality is quite different along those two directions due to the fact that along the modulation direction, $x \leftrightarrow k_x$, the MTF is convex. Whereas along the line focus direction, $y \leftrightarrow k_y$, the support is concave.

SFP tomographic imaging solves the issue of anisotropic imaging resolution — producing isotropic resolution in the x–y plane for lateral tomographies and in the x–z plane for FDT. LT images compared against the related conventional imaging methods produce superior imaging properties with single pixel SFP tomographic imaging. In Fig. (14 (a–c)), we compare first order SPIFI imaging with coherent widefield microscopy, which both exhibit cutoff spatial frequencies of k_c. Here, conventional widefield coherent imaging is superior to first-order SPIFI imaging Fig. (14 (a, c, d)). This situation changes for all higher order SPIFI imaging modes. Fig. (14 (b, d, f)), compares second order SPIFI imaging with incoherent widefield microscopy, both of which have a cutoff spatial frequency of $2\,k_c$. Despite having the same cutoff spatial frequency, the image formed for second order SPIFI is able to resolve much finer detail than is observed in the widefield incoherent image.

A similar trend is observed for nonlinear imaging. Fig. (15 (a–c)), compares the images for the case of two photon excitation fluorescence (TPEF) microscopy to the relevant SPIFI order, 4th order. Again, the same cutoff spatial frequencies are obtained in each case, yet the higher amplitude of the OTF for the SPIFI spatial frequency support provides a vastly superior image. This behavior is further amplified when we move to a three photon excitation fluorescence (3PEF) microscopy that is compared with 6th order SPIFI as shown in Fig. (15 (d–f)). Here again, the SPIFI image is vastly superior to the 3PEF image, with a higher amplitude of the OTF throughout the range of spatial frequencies.

6.2. Analytic inverse operators enable imaging of large fields of view

Single pixel imaging always requires an accurate forward model of both the illumination light patterns projected into the object and of the

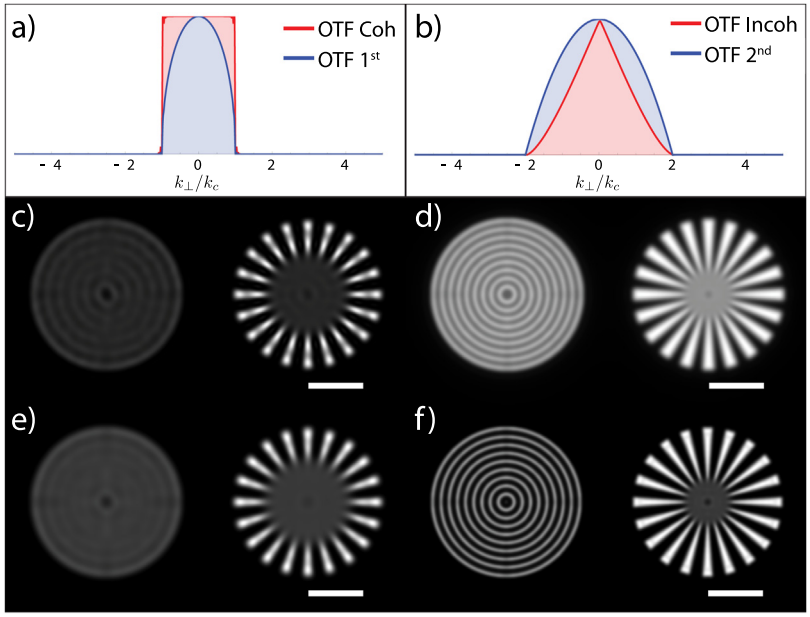

Fig. 14. A comparison of conventional linear microscopy to the related linear SPIFI. (a) Shows the OTF of coherent widefield microscopy (red line) and the first order SPIFI OTF (blue line). (b) Shows the incoherent widefield OTF (red line) and the second order SPIFI OTF (blue line). (c) Simulated images of coherent widefield. (d) Simulated images of incoherent widefield. (e) Simulated image of first order SPIFI. (f) Simulated image of second order SPIFI. The impact of the convex SPIFI spatial frequency support is evident in the higher image quality for the SPIFI images. The scale bar is 10 μm.

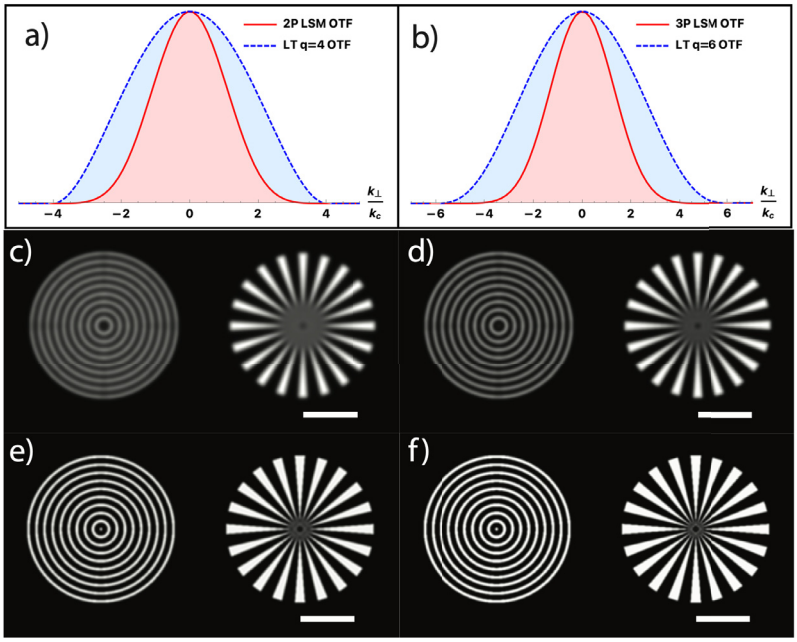

Fig. 15. A comparison of nonlinear laser scanning (LSM) to the related SPIFI order. (a) The OTF and (c) image for 2PEF LSM imaging (solid line with red shading), (a) the OTF and (d) image for fourth order SPIFI (dashed line with blue shading). (b) The OTF and (d) image for 3PEF LSM imaging (solid line with red shading), (b) the OTF and (f) image for sixth order SPIFI (dashed line with blue shading). The impact of the convex SPIFI spatial frequency support is evident in the higher image quality for the SPIFI images. The scale bar is 10 μm.

signal generation mechanism and collection. Such physical models can be instantiated in a discrete form as a measurement matrix to enable an estimate of the object from a discrete set of data measurements by minimizing the error provided by some norm, as shown in Eq. (1). While it is common to apply optimization algorithms for the estimation of an object, one runs into computational difficulties rather quickly for practical computational imaging scenarios. When possible, one should seek analytic inverse operators for image estimation.

Inverse operators must be found by seeking a kernel for an inverse operator that forms a biorthogonal relationship with the kernel in the forward operator integral. Mathematically a true inverse operator requires strict biorthogonality. However, in any far-field optical imaging system, where the light propagates to a detector at a distance more than several wavelengths away from the object, the transverse spatial frequency support only supports those spatial frequencies that propagate homogeneously, and evanescent waves with a spatial frequency higher than $2\pi\lambda^{-1}$ do not propagate to the far-field. Moreover, optical imaging almost always use optical lenses that further restricts the transverse spatial frequencies that participate in the image formation process. In most systems, the optical components act as a low pass spatial

frequency filter with a cutoff proportional to the numerical aperture. The restricted transverse spatial frequency support limits the range of integration in the forward and inverse models, making it so that the dual kernel in the inverse operator only forms a biorthogonal relationship in a limiting case of infinite spatial frequency support. To handle this subtlety, we have defined the full image estimate in terms of a function, $\beta(\tau)$, that expresses the PSF of the SFP computational imaging process as a weighted inner product of the forward operator kernel and the inverse operator dual kernel. Once the PSF is defined, the OTF readily follows. This ability to provide analytic models of the imaging proprieties of the computational imaging system is another benefit of finding an inverse operator. Unfortunately there is no guarantee that an analytic operator can be found, but in nearly all cases, such a strategy will have multiple benefits, such as reduced computation time, no storage of measurement matrices, and no hyper parameter tuning. To appreciate the power of analytic inverse operators, we consider the computational imaging problems of LT, FCT, and GTT.

6.3. Coherent imaging with incoherent light emission

One remarkable capability of single pixel SFP imaging is the ability to perform coherent imaging techniques with incoherent light emission (or incoherent scattering) [21,33]. We will take fluorescent light emission as an exemplar for incoherent light for SFP imaging, however, incoherent scattering or absorption can also be imaged with an equivalent strategy. In a single pixel fluorescent imaging experiment, a three dimensional light intensity distribution can illuminate a large volume in an object containing some distribution of fluorescent molecules. The influence of the propagation of the modulated illumination light in three dimensions depends on the coherence of the detected light. In experiments to date, SFP imaging has used spatially coherent light, but coherent light is not strictly necessary in all cases.

The differences between imaging with coherent and incoherent light are significant. Incoherent light is spatially incoherent, which means that the random phase fluctuations of the emitted light causes a loss of any link between the input illumination light direction and the emitted light. In contrast, when coherent light interacts with a scattering object, the scattered light carries specific direction, amplitude, and phase information that allows for the spatial distribution of the scatter to be computed by accounting for the differences between the illumination and scattered complex light fields.

The powerful properties of coherent imaging can be recovered when imaging incoherent light emission by employing a strategy in which we impart a spatially and temporally varying modulation of coherent light that is used to illuminate the three dimensional region containing the object (here the spatial distribution of the fluorescent molecule concentration). When modulated coherent light drives an incoherent imaging contrast mechanism, such as fluorescent light emission or spontaneous Raman scattering, the signal power is proportional to the modulated intensity at the location of that part of the object. Thus, the object information is recovered by mapping the detected temporal emission pattern to the spatial location in which that same temporal intensity modulation has been imparted.

Here, we reviewed techniques that are based on the modulation of spatialy coherent illumination light composed of a sparse set of transverse illumination spatial frequencies that propagate through the object region. Because we rely on a model of the propagation of the illumination fields, we are able to recover a mathematically identical model for the image formation process as is relevant for imaging with coherent scattering. At each time instance only a few transverse spatial frequencies are present in the illumination pattern, but a sequence of illumination patterns are applied that then leads to a sampling of the full set of transverse spatial frequencies supported by the illumination objective. The intensity of the illumination beams depends on the interference of the set of sparse spatial frequencies of the modulated fields propagating through the object. The phase difference between the modulated fields thus drives a time-varying local intensity modulation in the signal power, the temporal signatures recorded on a single pixel detector label each spatial point in the illumination volume. By determining the amplitude of each temporal signature used to label a particular point in the volume, a 3D image can be estimated. Note that depending on the experimental design, we may measure a 1D, 2D, or a 3D image from the sequence of measurements. However, the lower dimensional images can be assembled into a 3D image by scanning along the unmodulated directions.

In the case of fully coherent light, in the limit of the plane wave model, see 2, where the transverse spatial frequency support for all field terms are vanishingly narrow so that it is described by a Dirac delta function, the propagating waves in the object spatial region will be described by plane waves, and the fringe visibility of the interfering plane wave fields of equal amplitude over all space. The optical path between the plane waves will be slightly different from one another as one beam scans across the other. The optical path difference between the illumination plane waves will create a relative phase shift, $\phi(t)$, between the plane waves causing an intensity modulation in the illumination volume, where each x–z location will have an identifiable modulation frequency and phase. The image formation process described here is able to mimic a coherent scattering process [21,33] because the single pixel SFP imaging records the spatial frequency values of the object spatial frequency that is obtained from the difference spatial frequency of the illumination waves. SFP is also able to uniquely isolate interference terms due to a relative phase shift between the modulation plane waves, $\varphi(t)$, that allows for separation of all of the interference terms the produce the intensity. Such phase shifting to isolate particular terms in the interference of fields is critical for all coherent phase imaging methods, including widefield versions based on holography or other interferometric configurations. The fluorescent emitters respond to the modulated intensity, allowing the phase difference between the propagating modulated illumination beams to be encoded onto the collected signal, thereby allowing the incoherent light to mimic the coherent illumination. This encoded phase information allows coherent imaging tools to be applied to incoherent emission such as numerical refocusing, holography, and optical diffraction tomography [21,33,53].

In an experiment, the fringe visibility and spatial extent of the modulated illumination light depends on the shape of the spatial frequency support for each radiant field term and the defocus plane, z. The detailed shape of this region of interference can be controlled with wavefront shaping [55]. The imaging axial field of view can be extended to be much larger than is possible with conventional imaging [21,55].

There are several other camera based strategies for mimicking coherent imaging with incoherent light which rely on a very different strategies than that used in CHIRPT and FDT. In these strategies, the self coherence of interference from a single fluorescent emitter is exploited by placing a diffraction optical component, such as a Fresnel zone plate or a two dimensional grating in the imaging path, so that differences in propagation distance from the emitter location in the object to a camera are encoded as an intensity modulation [57,58]. Alternately, a common path imaging Sagnac interferometer can be used for super-resolution imaging by exploiting the interferometric shifts based on axial position of the emitter [68]. In each of these methods, self interference and light diffraction is exploited to convert diffraction into an intensity pattern recorded on a camera. SFP methods exploit deterministic propagation differences in modulated illumination light to encode position information. Importantly, with SFP methods, since the detection is based on recording power with a single pixel detector, imaging in harsh environments with optical scattering can still be performed, where the self interference methods with a camera will be degraded because scattering will distort the self-interference diffraction.

Partially and fully spatially incoherent light can still be used for SFP imaging, but the three dimensional imaging behavior will significantly

differ from the fully coherent case. Partially coherent beam propagation can be described with an incoherent sum, i.e., a sum over intensities, of a coherent mode decomposition of the illumination field. The spatial location of points of constructive and destructive interference from the propagation of each modulated coherent mode will be different — leading to a filling smoothing out of the modulation depth. The exception is in the focal plane ($z = 0$) where the modulation pattern will be faithfully imaged, regardless of the spatial coherence of the source. The axial extent of the modulation of the fringes is reduced as the spatial coherence decreases.

6.4. Computational three dimensional imaging

In this review, we have discussed two methods of 2D single pixel SFP imaging, either in the plane transverse to the direction of propagation, or in a plane with one transverse coordinate and the axial propagation direction. Three dimensional imaging is obtained by scanning along an additional dimension. There is strong interest in extending these methods directly to three dimensional imaging.

The direct extension of computational imaging to three dimensions can present a significant challenge. Deconvolution of stacks of axially displaced images for 3D computational imaging is possible for spatially incoherent (e.g., widefield fluorescent microscopy [69]), temporally incoherent [70], partially spatially coherent [71–73], and nonlinear widefield holography [74]. However, these methods all rely on camera acquisition, restricting their use to specimens with low levels of optical scattering. In addition, direct widefield imaging reduces the imaging problem because the problem may be modeled as a linear and shift invariant system, so that the impulse response function and the forward model may be represented sparsely in the spatial frequency domain by a transfer function.

In imaging systems where the forward operator is not represented by a sparse operator, the computation problem rapidly becomes untenable. A simple strategy is to layer 2D images to build a 3D image [33] or with a line detector that reads out SFP image in parallel, but this strategy provides limited resolution along the direction that the images are stacked. Alternatively, a one can apply sparsity constraints to the reconstruction of images recorded with a random diffuser lens [47].

6.5. SFP imaging speed

An important property of any imaging modality is the speed at which images may be acquired. Imaging with a single pixel detector is limited by the electronic detector bandwidth and required scanning. Part of the motivation of SFP imaging is to improve imaging speed by reducing scanning requirements of the illumination beam. The extent to which imaging speed improvements can be realized then depends on the rate at which line images, in the case of SPIFI and CHIRPT, or higher dimensional modulation patterns, can be acquired with a signal level higher than the noise levels. As single pixel imaging is a multiplexed imaging method, the type of noise present in the detection strongly influences the impact of noise in the estimated image [27, 75]. In fact, in a case where we are limited by a noise model well represented by an additive Gaussian noise model, multiplexing, such as with SFP tomography, carries a significant advantage. However, when shot noise is dominant, dim object points are subject to noise contamination from bright points, and imaging is degraded without adequate mitigation of noise in the image reconstruction algorithm.

To determine an upper bound on the imaging speed for a fluorescent object, we compute the SNR of a CHIRPT line focus image of a single bright point. The point object is envisioned to be of the form of a dyed microsphere, where we have a concentration of c fluorescent molecules within a volume V, so that we have a total of $\mathcal{N} = c\,V$ total fluorescent molecules within the volume. We further suppose that the volume is smaller than the volume resolution element (voxel), and localized to a point $\mathbf{r}_0$. To estimate the signal and noise levels, we first compute the detected photon flux. Assuming that the combination of collection optics and detector efficiency provides an overall detection efficiency of the emitted photons of η, we may write the detected photon flux for this CHIRPT imaging scenario as

$$\phi_d(\tau) = \eta\,\mathcal{N}\,k_r\,e_{\mathbf{r}_0}(\tau). \tag{41}$$

Here $\tau = t/T$ is the normalized CHIRPT modulation scan time and $k_r = 1/\tau_e$ is the radiative emission rate of the molecule with τ_e denoting the excited state lifetime.

The fluorescent emission is proportional to the excited state occupation population $e_{\mathbf{r}_0}(\tau)$. For the case of a three-level molecular system illuminated by cw laser, average excited state population is

$$e_{\mathbf{r}_0}(\tau) = \frac{I_{\text{ill}}(\mathbf{r}_0,\tau)\,I_{\text{sat}}^{-1}}{1 + I_{\text{ill}}(\mathbf{r}_0,\tau)\,I_{\text{sat}}^{-1}}, \tag{42}$$

where the saturation intensity is given by $I_{\text{sat}} = h\,\nu_a/\sigma_a\,\tau_e$. Here h is Planck's constant, ν_a is the optical absorption frequency, and σ_a is the absorption cross section at the illumination optical wavelength $\lambda_a = c/\nu_a$. To simplify notation, we define the peak saturation parameter at the spatial position $\mathbf{r}_0$ as $\alpha_0 = I_0/I_{\text{sat}}$. Here, the peak illumination intensity, I_0, at the object position $\mathbf{r}_0$ in the CHIRPT illumination intensity is $I_{\text{ill}}(\mathbf{r}_0,\tau) = I_0\,s_n(\mathbf{r}_0,\tau)$, with the normalized intensity modulation signal expressed as

$$s_n(\mathbf{r}_0,\tau) = \frac{1}{4}\left(2 + \tau^2 + \sqrt{1-\tau^2}\,\cos[\Omega_0\,\tau]\right). \tag{43}$$

Here $\Omega_0 = (\omega_m + \gamma x_0)\,T$ is the normalized CHIRPT modulation frequency at $\mathbf{r}_0$, and assuming one-dimensional modulation along the x direction. The time detected fluorescent photon flux may now be expressed as

$$\phi_d(\tau) = \eta\,\alpha_0\,\mathcal{N}\,k_r\,\frac{s_n(\mathbf{r}_0,\tau)}{1 + \alpha_0\,s_n(\mathbf{r}_0,\tau)}. \tag{44}$$

The imaging speed is estimated by computing the signal-to-noise ratio (SNR) and determining a suitable SNR level where the signal rises above the noise. A minimum suitable value occurs for SNR = 1, and we set this as our imaging speed criterion. The SNR is given by SNR = N_s/σ_s. The number of detected signal photons for the point object is defined by the amplitude of the cosine projection of the detected photon flux,

$$N_s = T\int_{-1}^{1}\cos(\Omega_0\,\tau)\,\phi_d(\tau)\,d\tau. \tag{45}$$

Assuming that the noise is dominated by shot noise, the standard deviation in the noise is given by $\sigma_s = \sqrt{\langle N\rangle}$. Here the mean detected photon count is

$$\langle N\rangle = \int_{-1}^{1}\phi_d(\tau)\,d\tau. \tag{46}$$

Analytic solutions to the signal photon integrals in Eqs. (45), (46) have not been found, however the following approximations produce only a small error when compared to a full numerical integration. An approximate signal value is obtained by taking a Taylor series expansion of the detected photon flux to second order in α_0, then integrating over the signal trace. The approximate signal found in this manner is given by

$$N_s \approx \frac{\pi}{16}\,\eta\,\alpha_0\,\mathcal{N}\,\frac{k_r}{\nu_{\text{img}}}\left(1 - \frac{9}{8}\,\alpha_0 + \frac{141}{128}\,\alpha_0^2\right). \tag{47}$$

This approximation only produces suitable results for $\alpha_0 < 0.5$. Here we have defined the imaging rate as $\nu_{\text{img}} = 1/2\,T$. An excellent approximation for the background signal level is found by computing the total photon count without the oscillatory portion of the normalized illumination intensity, leading to the expression

$$\langle N\rangle \approx \eta\,\mathcal{N}\,\frac{k_r}{\nu_{\text{img}}}\left(1 - \frac{2\sqrt{2}\cot^{-1}\left[\sqrt{2 + \frac{4}{\alpha_0}}\right]}{\sqrt{\alpha_0\,(2+\alpha_0)}}\right). \tag{48}$$

The two analytic expressions for the signal and total photon counts lead to an SNR expression of

$$\mathrm{SNR} \approx \sqrt{\eta \mathcal{N} \frac{k_r}{\nu_{\mathrm{img}}}}\, f_{\alpha_0}, \tag{49}$$

where

$$f_{\alpha_0} = \frac{\frac{\pi}{16}\left(1 - \frac{9}{8}\alpha_0 + \frac{141}{128}\alpha_0^2\right)}{\sqrt{\left(1 - \frac{2\sqrt{2}\cot^{-1}\left[\sqrt{2+\frac{4}{\alpha_0}}\right]}{\sqrt{\alpha_0(2+\alpha_0)}}\right)}}. \tag{50}$$

For small values of α_0, we have the approximation

$$f_{\alpha_0} \approx \frac{\pi}{8}\sqrt{\frac{3}{7}\alpha_0\left(1 - \frac{58}{35}\alpha_0\right)}. \tag{51}$$

With this expression, we may estimate the maximum imaging rate to second order in α_0 as

$$\nu_{\mathrm{img}} < \frac{3}{7}\left(\frac{\pi}{8}\right)^2 \alpha_0 \eta \mathcal{N} k_r \left(1 - \frac{58}{35}\alpha_0\right). \tag{52}$$

Taking some typical values for a set of $\mathcal{N} = 1000$ fluorescent molecules with a lifetime of $\tau_e = 4$ ns and an excitation strength of $\alpha_0 = 0.01$ and with a total detection efficiency of $\eta = 0.1$, then the upper bound on the line imaging rate is 16 MHz. Which means a 250 × 250 pixel 2D image could be acquired as fast as 660 kHz. Experimental implementation details will impose other constraints, but the photon detection rate does not preclude exceptionally fast imaging. Moreover, if bright-field imaging is used, where photon counts are much higher, then even faster imaging rates are theoretically accessible.

7. Conclusions

Single pixel imaging with spatial frequency projections provides a framework that enables new capabilities for optical imaging. By passing a sparse set of spatial frequencies through the CTF of the illumination optics, the delicate superposition of the plane waves from a broad range of spatial frequencies need not be maintained. As a result, the imaging field of view is readily expanded by more than an order of magnitude, and aberrations present in the imaging system are encoded in the measurement. These encoded aberrations can then be extracted and used to correct for system aberrations.

The sparse set of illumination spatial frequencies suffers less attenuation of the spatial frequencies that are passed to the object for incoherent imaging and a doubling of the range of spatial frequency support for coherent imaging. Moreover, the amplitude of the spatial frequency support, described by the modulation transfer function (MTF), is higher for high spatial frequencies than what is possible in conventional widefield imaging. Thus, even when the maximum spatial frequency value (the cutoff spatial frequency) between SFP imaging and widefield is the same, the image quality in SFP can be much better. The improvement in image quality is evident in Figs. 14, 15.

When driving a nonlinear response, the periodic sparse illumination intensity drives harmonics of the input spatial frequencies. These harmonics produce higher harmonic orders that expand the spatial frequency support beyond the capabilities of conventional laser scanning nonlinear optical microscopy [25] (see Fig. 15). Moreover, the amplitude of the MTF for nonlinear SFP imaging is improved compared to conventional nonlinear interactions. The result is vastly improved image quality, with the ability to resolve much finer details.

As SFP implemented as SPIFI or CHIRPT normally only improves image quality along the direction of spatial frequency modulation. To extend imaging improvements along two dimensions, one can either apply dual modulations [20], multiple line cursors [26], or through the use of tomography [33,48,49]. This review focuses on the imaging properties of tomographic imaging. Forward and inverse operators are derived for many experimental scenarios — enabling the calculation of the imaging impulse response, the PSF, and frequency transfer function, the OTF, for many cases. Image quality is shown to be significantly better than with conventional widefield or laser scanning imaging methodologies.

Computational imaging is a powerful strategy for expanding the capabilities of optical microscopy. By relaxing the requirement to form an optical image that is directly sampled by an array detector, the imaging system is freed from conventional microscope constraints, enabling a much broader range of imaging system design strategies. We discuss a few examples of benefits of single pixel SFP imaging, where much larger fields of view can be imaged with superior imaging quality. In addition, spectroscopic information can be multiplexed into the modulation by exploiting unused region of the bandwidth of the single pixel detector.

The challenge in computational imaging is that image estimation is computationally burdensome as the problem scales in size, particularly with the introduction of higher order dimensions. We have sought analytic inverse operators to avoid the need for entering large matrices into computer memory. While not all SFP imaging scenarios have a full inverse operator, this is an area of significant interest to move forward in order to further scale this imaging technology.

Declaration of competing interest

The authors declare that they have no known competing financial interests or personal relationships that could have appeared to influence the work reported in this paper.

Acknowledgments

We acknowledge funding support from the National Institute of Health (NIH), USA (R21EB025389, R21MH117786). J. Squier is supported by the National Science Foundation (NSF), USA (1707287).

References

[1] J. Mertz, Introduction to Optical Microscopy, second ed., Cambridge University Press, 2019, http://dx.doi.org/10.1017/9781108552660.
[2] J. Girkin, A Practical Guide to Optical Microscopy, first ed., CRC Press, 2019, http://dx.doi.org/10.1017/9781138064706.
[3] A. Karim, J.Y. Andersson, Infrared detectors: Advances, challenges and new technologies, IOP Conf. Ser.: Mater. Sci. Eng. 51 (2013) 012001, http://dx.doi.org/10.1088/1757-899x/51/1/012001.
[4] R.A. Lewis, A review of terahertz detectors, J. Phys. D: Appl. Phys. 52 (43) (2019) 433001, http://dx.doi.org/10.1088/1361-6463/ab31d5.
[5] J. Pawley (Ed.), Handbook of Biological Confocal Microscopy, third ed., Springer-Verlag US, 2006, http://dx.doi.org/10.1007/978-0-387-45524-2.
[6] E.E. Hoover, J.A. Squier, Advances in multiphoton microscopy technology, Nat. Photonics 7 (2) (2013) 93–101, http://dx.doi.org/10.1038/nphoton.2012.361.
[7] M.D. Young, J.J. Field, K.E. Sheetz, R.A. Bartels, J. Squier, A pragmatic guide to multiphoton microscope design, Adv. Opt. Photon. 7 (2) (2015) 276–378, http://dx.doi.org/10.1364/AOP.7.000276, URL http://aop.osa.org/abstract.cfm?URI=aop-7-2-276.
[8] E.E. Hoover, J.J. Field, D.G. Winters, M.D. Young, E.V. Chandler, J.C. Speirs, J.T. Lapenna, S.M. Kim, S.-Y. Ding, R.A. Bartels, J.W. Wang, J.A. Squier, Eliminating the scattering ambiguity in multifocal, multimodal, multiphoton imaging systems, J. Biophotonics 5 (5–6) (2012) 425–436, http://dx.doi.org/10.1002/jbio.201100139, URL https://pubmed.ncbi.nlm.nih.gov/22461190.
[9] A. Buist, M. Müller, J. Squier, G. Brakenhoff, et al., Real-time two-photon absorption microscopy using multi point excitation, J. Microsc. 192 (1998).
[10] J. Bewersdorf, R. Pick, S.W. Hell, Multifocal multiphoton microscopy, Opt. Lett. 23 (9) (1998) 655–657, http://dx.doi.org/10.1364/OL.23.000655, URL http://ol.osa.org/abstract.cfm?URI=ol-23-9-655.
[11] G. Futia, P. Schlup, D.G. Winters, R.A. Bartels, Spatially-chirped modulation imaging of absorbtion and fluorescent objects on single-element optical detector, Opt. Express 19 (2) (2011) 1626–1640, http://dx.doi.org/10.1364/OE.19.001626, URL http://www.opticsexpress.org/abstract.cfm?URI=oe-19-2-1626.
[12] E.E. Hoover, M.D. Young, E.V. Chandler, A. Luo, J.J. Field, K.E. Sheetz, A.W. Sylvester, J.A. Squier, Remote focusing for programmable multi-layer differential multiphoton microscopy, Biomed. Opt. Express 2 (1) (2011) 113–122, http://dx.doi.org/10.1364/BOE.2.000113, URL http://www.osapublishing.org/boe/abstract.cfm?URI=boe-2-1-113.

[13] M. Ingaramo, A.G. York, P. Wawrzusin, O. Milberg, A. Hong, R. Weigert, H. Shroff, G.H. Patterson, Two-photon excitation improves multifocal structured illumination microscopy in thick scattering tissue, Proc. Natl. Acad. Sci. 111 (14) (2014) 5254–5259, http://dx.doi.org/10.1073/pnas.1314447111, arXiv:https://www.pnas.org/content/111/14/5254.full.pdf.

[14] M. Harwit, N.J. Sloane, Chapter 3 - The basic theory of Hadamard transform spectrometers and imagers, in: M. Harwit, N.J. Sloane (Eds.), Hadamard Transform Optics, Academic Press, 1979, pp. 44–95, http://dx.doi.org/10.1016/B978-0-12-330050-8.50007-X, URL https://www.sciencedirect.com/science/article/pii/B978012330050850007X.

[15] A. Gatti, E. Brambilla, M. Bache, L.A. Lugiato, Ghost imaging with thermal light: Comparing entanglement and ClassicalCorrelation, Phys. Rev. Lett. 93 (2004) 093602, http://dx.doi.org/10.1103/PhysRevLett.93.093602, URL https://link.aps.org/doi/10.1103/PhysRevLett.93.093602.

[16] J.H. Shapiro, Computational ghost imaging, Phys. Rev. A 78 (2008) 061802, http://dx.doi.org/10.1103/PhysRevA.78.061802, URL https://link.aps.org/doi/10.1103/PhysRevA.78.061802.

[17] O. Katz, Y. Bromberg, Y. Silberberg, Compressive ghost imaging, Appl. Phys. Lett. 95 (13) (2009) 131110, http://dx.doi.org/10.1063/1.3238296.

[18] M.J. Padgett, R.W. Boyd, An introduction to ghost imaging: quantum and classical, Phil. Trans. R. Soc. A 375 (2099) (2017) 20160233, http://dx.doi.org/10.1098/rsta.2016.0233, arXiv:https://royalsocietypublishing.org/doi/pdf/10.1098/rsta.2016.0233.

[19] M.F. Duarte, M.A. Davenport, D. Takhar, J.N. Laska, T. Sun, K.F. Kelly, R.G. Baraniuk, Single-pixel imaging via compressive sampling, IEEE Signal Process. Mag. 25 (2) (2008) 83–91, http://dx.doi.org/10.1109/MSP.2007.914730.

[20] D.G. Winters, R.A. Bartels, Two-dimensional single-pixel imaging by cascaded orthogonal line spatial modulation, Opt. Lett. 40 (12) (2015) 2774–2777, http://dx.doi.org/10.1364/OL.40.002774, URL http://ol.osa.org/abstract.cfm?URI=ol-40-12-2774.

[21] J.J. Field, D.G. Winters, R.A. Bartels, Single-pixel fluorescent imaging with temporally labeled illumination patterns, Optica 3 (9) (2016) 971–974, http://dx.doi.org/10.1364/OPTICA.3.000971, URL http://www.osapublishing.org/optica/abstract.cfm?URI=optica-3-9-971.

[22] E. Block, M.D. Young, D.G. Winters, J.J. Field, R.A. Bartels, J.A. Squier, Simultaneous spatial frequency modulation imaging and micromachining with a femtosecond laser, Opt. Lett. 41 (2) (2016) 265–268, http://dx.doi.org/10.1364/OL.41.000265, URL http://ol.osa.org/abstract.cfm?URI=ol-41-2-265.

[23] R.G. Baraniuk, Compressive sensing [lecture notes], IEEE Signal Process. Mag. 24 (4) (2007) 118–121, http://dx.doi.org/10.1109/MSP.2007.4286571.

[24] J. Romberg, Imaging via compressive sampling, IEEE Signal Process. Mag. 25 (2) (2008) 14–20, http://dx.doi.org/10.1109/MSP.2007.914729.

[25] J.J. Field, K.A. Wernsing, S.R. Domingue, A.M. Allende Motz, K.F. DeLuca, D.H. Levi, J.G. DeLuca, M.D. Young, J.A. Squier, R.A. Bartels, Superresolved multiphoton microscopy with spatial frequency-modulated imaging, Proc. Natl. Acad. Sci. 113 (24) (2016) 6605–6610, http://dx.doi.org/10.1073/pnas.1602811113, arXiv:https://www.pnas.org/content/113/24/6605.full.pdf.

[26] N. Worts, J. Field, R. Bartels, J. Jones, J. Broderick, J. Squier, Interferometric spatial frequency modulation imaging, Opt. Lett. 43 (21) (2018) 5351–5354, http://dx.doi.org/10.1364/OL.43.005351, URL http://ol.osa.org/abstract.cfm?URI=ol-43-21-5351.

[27] S. Heuke, S. Sivankutty, C. Scotte, P. Stockton, R.A. Bartels, A. Sentenac, H. Rigneault, Spatial frequency modulated imaging in coherent anti-Stokes Raman microscopy, Optica 7 (5) (2020) 417–424, http://dx.doi.org/10.1364/OPTICA.386526, URL http://www.osapublishing.org/optica/abstract.cfm?URI=optica-7-5-417.

[28] S.R. Domingue, D.G. Winters, R.A. Bartels, Hyperspectral imaging via labeled excitation light and background-free absorption spectroscopy, Optica 2 (11) (2015) 929–932, http://dx.doi.org/10.1364/OPTICA.2.000929, URL http://www.osapublishing.org/optica/abstract.cfm?URI=optica-2-11-929.

[29] S.R. Domingue, R.A. Bartels, General theoretical treatment of spectral modulation light-labeling spectroscopy, J. Opt. Soc. Amer. B 33 (6) (2016) 1216–1224, http://dx.doi.org/10.1364/JOSAB.33.001216, URL http://josab.osa.org/abstract.cfm?URI=josab-33-6-1216.

[30] C. Scotté, S. Sivankutty, P. Stockton, R.A. Bartels, H. Rigneault, Compressive Raman imaging with spatial frequency modulated illumination, Opt. Lett. 44 (8) (2019) 1936–1939, http://dx.doi.org/10.1364/OL.44.001936, URL http://ol.osa.org/abstract.cfm?URI=ol-44-8-1936.

[31] C. Scotté, S. Sivankutty, R.A. Bartels, H. Rigneault, Line-scan compressive Raman imaging with spatiospectral encoding, Opt. Lett. 45 (19) (2020) 5567–5570, http://dx.doi.org/10.1364/OL.400151, URL http://ol.osa.org/abstract.cfm?URI=ol-45-19-5567.

[32] P.A. Stockton, J.J. Field, R.A. Bartels, Single pixel quantitative phase imaging with spatial frequency projections, Methods 136 (2018) 24–34, http://dx.doi.org/10.1016/j.ymeth.2017.10.007, Methods in Quantitative Phase Imaging in Life Science, URL https://www.sciencedirect.com/science/article/pii/S1046202317301755.

[33] P.A. Stockton, J.J. Field, J. Squier, A. Pezeshki, R.A. Bartels, Single-pixel fluorescent diffraction tomography, Optica 7 (11) (2020) 1617–1620, http://dx.doi.org/10.1364/OPTICA.400547, URL http://www.osapublishing.org/optica/abstract.cfm?URI=optica-7-11-1617.

[34] M. Torabzadeh, I.-Y. Park, R.A. Bartels, A.J. Durkin, B.J. Tromberg, Compressed single pixel imaging in the spatial frequency domain, J. Biomed. Opt. 22 (3) (2017) 1–4, http://dx.doi.org/10.1117/1.JBO.22.3.030501.

[35] M. Torabzadeh, P.A. Stockton, G.T. Kennedy, R.B. Saager, A.J. Durkin, R.A. Bartels, B.J. Tromberg, Hyperspectral imaging in the spatial frequency domain with a supercontinuum source, J. Biomed. Opt. 24 (7) (2019) 1–9, http://dx.doi.org/10.1117/1.JBO.24.7.071614.

[36] J.S. Sanders, R.G. Driggers, C.E. Halford, S.T. Griffin, Imaging with frequency-modulated reticles, Opt. Eng. 30 (11) (1991) 1720–1724, http://dx.doi.org/10.1117/12.55994.

[37] W.L. Chan, K. Charan, D. Takhar, K.F. Kelly, R.G. Baraniuk, D.M. Mittleman, A single-pixel terahertz imaging system based on compressed sensing, Appl. Phys. Lett. 93 (12) (2008) 121105, http://dx.doi.org/10.1063/1.2989126.

[38] M. Harwit, N.J. Sloane, Chapter 4 - noise or when to multiplex and when to avoid it, in: M. Harwit, N.J. Sloane (Eds.), Hadamard Transform Optics, Academic Press, 1979, pp. 96–108, http://dx.doi.org/10.1016/B978-0-12-330050-8.50008-1, URL https://www.sciencedirect.com/science/article/pii/B9780123300508500081.

[39] E. Voigtman, J.D. Winefordner, The multiplex disadvantage and excess low-frequency noise, Appl. Spectrosc. 41 (7) (1987) 1182–1184, http://dx.doi.org/10.1366/0003702874447509.

[40] E. Thiébaut, Introduction toimage reconstruction and inverse problems, in: R. Foy, F.C. Foy (Eds.), Optics in Astrophysics, Springer Netherlands, Dordrecht, 2005, pp. 397–422.

[41] P. Sarder, A. Nehorai, Deconvolution methods for 3-D fluorescence microscopy images, IEEE Signal Process. Mag. 23 (3) (2006) 32–45, http://dx.doi.org/10.1109/MSP.2006.1628876.

[42] A. Ribes, F. Schmitt, Linear inverse problems in imaging, IEEE Signal Process. Mag. 25 (4) (2008) 84–99, http://dx.doi.org/10.1109/MSP.2008.923099.

[43] S. Boyd, L. Vandenberghe, Convex Optimization, Cambridge University Press, 2004, http://dx.doi.org/10.1017/CBO9780511804441.

[44] M. Bertero, M. Piana, Inverse Problems in Biomedical Imaging: Modeling and Methods of Solution, Springer Milan, Milano, 2006, pp. 1–33, http://dx.doi.org/10.1007/88-470-0396-2_1.

[45] U.S. Kamilov, I.N. Papadopoulos, M.H. Shoreh, A. Goy, C. Vonesch, M. Unser, D. Psaltis, Learning approach to optical tomography, Optica 2 (6) (2015) 517–522, http://dx.doi.org/10.1364/OPTICA.2.000517, URL http://www.osapublishing.org/optica/abstract.cfm?URI=optica-2-6-517.

[46] A. Sinha, J. Lee, S. Li, G. Barbastathis, Lensless computational imaging through deep learning, Optica 4 (9) (2017) 1117–1125, http://dx.doi.org/10.1364/OPTICA.4.001117, URL http://www.osapublishing.org/optica/abstract.cfm?URI=optica-4-9-1117.

[47] N. Antipa, G. Kuo, R. Heckel, B. Mildenhall, E. Bostan, R. Ng, L. Waller, Diffusercam: Lensless single-exposure 3D imaging, Optica 5 (1) (2018) 1–9, http://dx.doi.org/10.1364/OPTICA.5.000001, URL http://www.osapublishing.org/optica/abstract.cfm?URI=optica-5-1-1.

[48] P. Schlup, G. Futia, R.A. Bartels, Lateral tomographic spatial frequency modulated imaging, Appl. Phys. Lett. 98 (21) (2011) 211115, http://dx.doi.org/10.1063/1.3595305.

[49] P.A. Stockton, K.A. Wernsing, J.J. Field, J. Squier, R.A. Bartels, Fourier computed tomographic imaging of two dimensional fluorescent objects, APL Photonics 4 (10) (2019) 106102, http://dx.doi.org/10.1063/1.5100525.

[50] S.S. Howard, A. Straub, N. Horton, D. Kobat, C. Xu, Frequency multiplexed in vivo multiphoton phosphorescence lifetime microscopy, Nat. Photonics 7 (1) (2013) 33–37, http://dx.doi.org/10.1038/nphoton.2012.307, URL https://pubmed.ncbi.nlm.nih.gov/23472061.

[51] L. Novotny, B. Hecht, Principles of Nano-Optics, Cambridge University Press, 2006, http://dx.doi.org/10.1017/CBO9780511813535.

[52] D.J. Higley, D.G. Winters, G.L. Futia, R.A. Bartels, Theory of diffraction effects in spatial frequency-modulated imaging, J. Opt. Soc. Amer. A 29 (12) (2012) 2579–2590, http://dx.doi.org/10.1364/JOSAA.29.002579, URL http://josaa.osa.org/abstract.cfm?URI=josaa-29-12-2579.

[53] J.J. Field, D.G. Winters, R.A. Bartels, Plane wave analysis of coherent holographic image reconstruction by phase transfer (CHIRPT), J. Opt. Soc. Amer. A 32 (11) (2015) 2156–2168, http://dx.doi.org/10.1364/JOSAA.32.002156, URL http://josaa.osa.org/abstract.cfm?URI=josaa-32-11-2156.

[54] J.J. Field, K.A. Wernsing, J.A. Squier, R.A. Bartels, Three-dimensional single-pixel imaging of incoherent light with spatiotemporally modulated illumination, J. Opt. Soc. Amer. A 35 (8) (2018) 1438–1449, http://dx.doi.org/10.1364/JOSAA.35.001438, URL http://josaa.osa.org/abstract.cfm?URI=josaa-35-8-1438.

[55] J.J. Field, J.A. Squier, R.A. Bartels, Fluorescent coherent diffractive imaging with accelerating light sheets, Opt. Express 27 (9) (2019) 13015–13030, http://dx.doi.org/10.1364/OE.27.013015, URL http://www.opticsexpress.org/abstract.cfm?URI=oe-27-9-13015.

[56] P.S. Carney, J.C. Schotland, E. Wolf, Generalized optical theorem for reflection, transmission, and extinction of power for scalar fields, Phys. Rev. E 70 (2004) 036611, http://dx.doi.org/10.1103/PhysRevE.70.036611, URL https://link.aps.org/doi/10.1103/PhysRevE.70.036611.

[57] P. Bon, J. Linarès-Loyez, M. Feyeux, K. Alessandri, B. Lounis, P. Nassoy, L. Cognet, Self-interference 3D super-resolution microscopy for deep tissue investigations, Nature Methods 15 (6) (2018) 449–454, http://dx.doi.org/10.1038/s41592-018-0005-3.

[58] N. Yoneda, Y. Saita, T. Nomura, Motionless optical scanning holography, Opt. Lett. 45 (12) (2020) 3184–3187, http://dx.doi.org/10.1364/OL.393534, URL http://www.osapublishing.org/ol/abstract.cfm?URI=ol-45-12-3184.

[59] E. Wolf, Three-dimensional structure determination of semi-transparent objects from holographic data, Opt. Commun. 1 (4) (1969) 153–156, http://dx.doi.org/10.1016/0030-4018(69)90052-2, URL https://www.sciencedirect.com/science/article/pii/0030401869900522.

[60] 3. Algorithms For reconstruction with nondiffracting sources, in: Principles of Computerized Tomographic Imaging, pp. 49–112, http://dx.doi.org/10.1137/1.9780898719277.ch3, arXiv:https://epubs.siam.org/doi/pdf/10.1137/1.9780898719277.ch3.

[61] M. Bertero, P. Boccacci, Introduction to Inverse Problems in Imaging, CRC Press, 1998, http://dx.doi.org/10.1201/9780367806941.

[62] Chapter 2: Naive reconstructions and inverse crimes, in: Linear and Nonlinear Inverse Problems with Practical Applications, pp. 7–34, http://dx.doi.org/10.1137/1.9781611972344.ch2, arXiv:https://epubs.siam.org/doi/pdf/10.1137/1.9781611972344.ch2.

[63] A. Beck, M. Teboulle, A fast iterative shrinkage-thresholding algorithm for linear inverse problems, SIAM J. Img. Sci. 2 (1) (2009) 183–202, http://dx.doi.org/10.1137/080716542.

[64] C.J.R. Sheppard, S.B. Mehta, R. Heintzmann, Superresolution by image scanning microscopy using pixel reassignment, Opt. Lett. 38 (15) (2013) 2889–2892, http://dx.doi.org/10.1364/OL.38.002889, URL http://ol.osa.org/abstract.cfm?URI=ol-38-15-2889.

[65] S. Roth, C.J. Sheppard, K. Wicker, R. Heintzmann, Optical photon reassignment microscopy (OPRA), Opt. Nanoscopy 2 (1) (2013) 5, http://dx.doi.org/10.1186/2192-2853-2-5.

[66] G.M.D. Luca, R.M. Breedijk, R.A. Brandt, C.H. Zeelenberg, B.E. de Jong, W. Timmermans, L.N. Azar, R.A. Hoebe, S. Stallinga, E.M. Manders, Re-scan confocal microscopy: scanning twice for better resolution, Biomed. Opt. Express 4 (11) (2013) 2644–2656, http://dx.doi.org/10.1364/BOE.4.002644, URL http://www.osapublishing.org/boe/abstract.cfm?URI=boe-4-11-2644.

[67] C.J.R. Sheppard, M. Castello, G. Tortarolo, T. Deguchi, S.V. Koho, G. Vicidomini, A. Diaspro, Pixel reassignment in image scanning microscopy: a re-evaluation, J. Opt. Soc. Amer. A 37 (1) (2020) 154–162, http://dx.doi.org/10.1364/JOSAA.37.000154, URL http://josaa.osa.org/abstract.cfm?URI=josaa-37-1-154.

[68] J. Wang, E.S. Allgeyer, G. Sirinakis, Y. Zhang, K. Hu, M.D. Lessard, Y. Li, R. Diekmann, M.A. Phillips, I.M. Dobbie, J. Ries, M.J. Booth, J. Bewersdorf, Implementation of a 4pi-SMS super-resolution microscope, Nat. Protoc. 16 (2) (2021) 677–727, http://dx.doi.org/10.1038/s41596-020-00428-7.

[69] P. Sarder, A. Nehorai, Deconvolution methods for 3-D fluorescence microscopy images, IEEE Signal Process. Mag. 23 (3) (2006) 32–45, http://dx.doi.org/10.1109/MSP.2006.1628876.

[70] T. Kim, R. Zhou, M. Mir, S.D. Babacan, P.S. Carney, L.L. Goddard, G. Popescu, White-light diffraction tomography of unlabelled live cells, Nat. Photonics 8 (3) (2014) 256–263, http://dx.doi.org/10.1038/nphoton.2013.350.

[71] N. Streibl, Three-dimensional imaging by a microscope, J. Opt. Soc. Amer. A 2 (2) (1985) 121–127, http://dx.doi.org/10.1364/JOSAA.2.000121, URL http://josaa.osa.org/abstract.cfm?URI=josaa-2-2-121.

[72] M.H. Jenkins, T.K. Gaylord, Three-dimensional quantitative phase imaging via tomographic deconvolution phase microscopy, Appl. Opt. 54 (31) (2015) 9213–9227, http://dx.doi.org/10.1364/AO.54.009213, URL http://ao.osa.org/abstract.cfm?URI=ao-54-31-9213.

[73] M. Chen, L. Tian, L. Waller, 3D differential phase contrast microscopy, Biomed. Opt. Express 7 (10) (2016) 3940–3950, http://dx.doi.org/10.1364/BOE.7.003940, URL http://www.osapublishing.org/boe/abstract.cfm?URI=boe-7-10-3940.

[74] C. Hu, J.J. Field, V. Kelkar, B. Chiang, K. Wernsing, K.C. Toussaint, R.A. Bartels, G. Popescu, Harmonic optical tomography of nonlinear structures, Nat. Photonics 14 (9) (2020) 564–569, http://dx.doi.org/10.1038/s41566-020-0638-5.

[75] M. Harwit, N.J. Sloane, Chapter 4 - noise or when to multiplex and when to avoid it, in: M. Harwit, N.J. Sloane (Eds.), Hadamard Transform Optics, Academic Press, 1979, pp. 96–108, http://dx.doi.org/10.1016/B978-0-12-330050-8.50008-1, URL https://www.sciencedirect.com/science/article/pii/B9780123300508500081.